

1 **An Unusual Case of Rapid Cyclogenesis in the northeast Pacific Basin.**

2 **Overview and Piecewise PV Inversion.**

3 Patrick T. Beaty,^a Jonathan E. Martin,^a Andrew C. Winters,^b Gary M. Lackmann^c

4 ^a *University of Wisconsin-Madison*

5 ^b *University of Colorado-Boulder*

6 ^c *North Carolina State University*

7

8 Corresponding author: Patrick T. Beaty, pbeaty@wisc.edu

9

ABSTRACT

10 A case of extremely rapid, record-setting extratropical cyclogenesis over
11 the northeast Pacific Ocean in late November 2019 is examined. The
12 development is of particular interest as much of the strengthening occurred in an
13 unusual environment characterized by cold sea surface temperatures.
14 Cyclogenesis began as a stationary upstream surface cyclone in the north-central
15 Pacific ushered warm, moist tropical air poleward towards a pre-existing surface
16 frontal boundary, resulting in intense lower-tropospheric frontogenesis. The
17 resulting thermally direct vertical circulation mobilized a diabatic Rossby wave
18 (DRW) which moved eastward along the baroclinic zone. An intensifying upper-
19 level jet/front system draping equatorward from Alaska became favorably aligned
20 with the low-level DRW on its approach towards the California-Oregon border to
21 force deepening rates as high as 6 hPa hr^{-1} prior to landfall. The 3D Ertel
22 potential vorticity (PV) structure associated with this storm is partitioned into
23 separate upper-tropospheric, lower-tropospheric, and diabatically-induced
24 anomalies which are separately inverted to recover the flow associated with each
25 piece. Analysis of this partitioned PV reveals that development followed a
26 bottom-up sequence by which near-surface PV dominated early cyclogenesis,
27 diabatically-induced PV dominated a large period of subsequent intensification,
28 and upper-tropospheric PV dominated the final period of development. Bottom-
29 up developments of this intensity are rare. It is shown that diabatic influences in
30 response to vigorous latent heat release are responsible for much of the lower-
31 tropospheric cyclogenesis with an upper-level jet/front system becoming an
32 important driver for the rapid cyclogenesis observed immediately before landfall.

33

SIGNIFICANCE STATEMENT

34 A rapidly-developing low-pressure system over the northeast Pacific Ocean in
35 late November 2019 set all-time low pressure records and occurred in an unusual
36 region of the world. The analysis shows that this development occurred from the
37 bottom-up and mid-tropospheric latent heat release was the most important
38 process leading to its record strength. It is very uncommon for low-pressure

39 systems of this intensity to follow a bottom-up development. More work is
40 needed to determine how the upper- and lower-tropospheric features interacted
41 with each other as they conspired to produce this record-setting low-pressure
42 system.

43 **1. Introduction**

44 Rapid extratropical cyclogenesis, colloquially known as "bomb" cyclogenesis
45 (e.g., Sanders and Gyakum 1980; Roebber 1984) arises from a variety of different
46 dynamical and thermodynamical factors including the interaction between upper-
47 tropospheric troughs and lower-tropospheric baroclinic zones (e.g., Sanders 1986;
48 Gyakum et al. 1992; Lagouvardos et al. 2007; Heo et al. 2019), diabatic heating in the
49 form of latent heat release, (Bosart 1981; Roebber 1993; Martin and Otkin 2004;
50 Terpstra et al. 2015; Kohl and O’Gorman 2022) and/or sea-surface heat fluxes (e.g.,
51 Davis and Emanuel 1988; Roebber 1989; Kuo et al. 1991; Gyakum and Danielson
52 2000; Kouroutzoglou et al. 2015). In addition, the interaction between a diabatic
53 Rossby wave (DRW) and an upper-tropospheric trough (Wernli et al. 2002; Moore et
54 al. 2008; Rivière et al. 2010; Boettcher and Wernli 2011, 2013; McKenzie 2014;
55 Tamarin and Kaspi 2016; Zhang and Wang 2018) is a particular kind of rapid
56 cyclogenesis event. The concept of a DRW was introduced in a series of studies in the
57 early 1990s (i.e., Raymond and Jiang 1990; Snyder and Lindzen 1991; Parker and
58 Thorpe 1995). The latter two studies employed highly idealized models with cloud-
59 diabatic feedbacks in the vicinity of lower-troposphere baroclinic zones to consider
60 both the production, and subsequent evolution, of positive low-level potential
61 vorticity (PV) anomalies beneath the location of maximum cloud production.

62 Studies by Moore and Montgomery (2004, 2005) were the first to classify such
63 low-level PV anomalies as diabatically-generated vortices. The interaction between
64 the associated cyclonic flow around such a vortex and the baroclinic zone along
65 which it forms acts to provide continued positive moisture and temperature advections
66 downstream of the vortex. These advections contribute to the production of clouds

67 and precipitation, which regenerate the lower-tropospheric cyclonic PV anomaly
68 downstream, thereby appearing to propagate the original anomaly downstream
69 (Terpstra et al. 2015; Tamarin and Kaspi 2016; Kohl and O’Gorman 2022).

70 In late December 1999, storm *Lothar* devastated portions of western Europe,
71 becoming the costliest windstorm in European history in terms of structural and
72 ecological damage (Wernli et al. 2002). Focusing their analysis of the event on the
73 evolution of *Lothar* as a DRW, Wernli et al. (2002) showed that *Lothar* underwent a
74 ‘bottom-up’ development in which the lower-tropospheric cyclonic PV anomaly (the
75 DRW), acting on an initially zonal upper-tropospheric flow, induced upper-
76 tropospheric trough development which eventually enabled a superposition of upper-
77 and lower-tropospheric PV features. Though bottom-up development of explosive
78 DRWs with no pre-existing upper-tropospheric trough is rare (Boettcher and Wernli
79 2013), such a configuration served to initiate the mutual amplification of the two
80 features which was manifest in the rapid development of *Lothar*. Rivière et al. (2010)
81 employed the Météo-France operational model to perform a sensitivity analysis on the
82 development of *Lothar* and, though analysis was centered around the investigation of
83 *Lothar*, the conclusions were extended to explosive development of DRWs in general.
84 They found that the explosive growth stage of rapidly developing DRWs such as
85 *Lothar* are highly dependent on 1) moist processes to overcome frictional and
86 turbulent dissipation, 2) the location of the upper-tropospheric jet exit region to aid in
87 synoptic-scale ascent, and 3) a lower-tropospheric baroclinic zone to encourage DRW
88 self-sustenance.

89 Boettcher and Wernli (2011) used four European Centre for Medium-Range
90 Weather Forecasts (ECMWF) model forecasts initialized at different lead times along
91 with a DRW-tracking algorithm to interrogate the influence of downstream lower-
92 tropospheric temperature and moisture advections on rapid DRW developments.
93 Boettcher and Wernli (2013) constructed a 10-year climatology of DRWs in the
94 Northern Hemisphere based on the tracking algorithm developed in Boettcher and
95 Wernli (2011). These consecutive studies led to the identification of four precursor
96 environments favorable for DRW genesis: 1) a broad subtropical high advecting
97 warm air and moisture towards a baroclinic zone, 2) a cutoff low or remnant tropical

98 cyclone advecting warm air and moisture towards a baroclinic zone, 3) an upper-
99 tropospheric trough moving over a lower-tropospheric baroclinic zone, and 4) the
100 remnants of a tropical cyclone or mesoscale convective system propagating along a
101 baroclinic zone as a lower-tropospheric vortex. Frequent locations of rapid DRW
102 developments in the Northern Hemisphere were along the Gulf Stream in the Atlantic
103 Ocean and following the climatological North Pacific wintertime jet (Boettcher and
104 Wernli 2013). In addition, they suggested that most cases of explosive DRW
105 development involve a DRW interacting with a pre-existing upper-tropospheric
106 trough.

107 Moore et al. (2008) and Rivière et al. (2010) both took advantage of the utility
108 of the piecewise PV inversion method introduced by Davis and Emanuel (1991) to
109 attribute the intensification of a DRW cyclogenesis event to discrete pieces of the full
110 column PV. The cases chosen for both studies were DRWs propagating over warm
111 sea surface temperatures (SSTs) which provides substantial surface heat and moisture
112 fluxes to aid in the rapid strengthening of the DRW (e.g., Davis and Emanuel 1988;
113 Roebber 1989; Kuo et al. 1991; Gyakum and Danielson 2000; Kouroutzoglou et al.
114 2015). To the best of the authors' knowledge, a similar analysis on an explosive DRW
115 development over a cold ocean surface ($< 12^{\circ}\text{C}$) has not yet been performed. DRW
116 developments over such cold ocean surfaces represented an estimated 5% of *all*
117 tracked DRWs in the Boettcher and Wernli (2013) climatology.

118 From 0000 UTC 26 November to 0000 UTC 27 November 2019, a DRW,
119 originating at the intersection of a high θ_e tropical moisture plume and a zonally
120 oriented baroclinic zone, underwent rapid cyclogenesis over the northeast Pacific
121 Ocean. DRW intensification followed the description offered by Boettcher and Wernli
122 (2013), wherein low-level diabatically-generated PV associated with the DRW vortex
123 became vertically collocated with an upper-tropospheric PV anomaly borne of a
124 downward and equatorward surge of stratospheric air. Hourly ECMWF reanalysis
125 version 5 (ERA5; Hersbach et al. 2020) data suggest that this superposition of
126 forcings resulted in a remarkable mean sea level pressure (MSLP) fall of 49 hPa in 24
127 hours as the DRW progressed east-southeastward towards the United States West
128 Coast. As the storm neared landfall, the MSLP dropped 12 hPa between 1600 UTC

129 and 1900 UTC 26 November, including a 1-hour central MSLP fall of 6 hPa from
130 1700 UTC to 1800 UTC 26 November 2019. The observed MSLP minimum of 973.4
131 hPa at Crescent City, California at 0300 UTC 27 November 2019 set the all-time low
132 sea-level pressure record for the state of California. November low sea-level pressure
133 records were also observed in Medford, Oregon (981.4 hPa) and Eureka, California
134 (984.4 hPa) on the same date.

135 The November 2019 (hereafter NV19) cyclone provides an opportunity to
136 interrogate the nature of an explosive DRW development over a cold ocean surface.
137 The analysis will center on a piecewise PV inversion of this particular cyclone
138 following the method of Davis and Emanuel (1991). Comparing this event to those
139 previously examined (over warm SSTs) will highlight physical precursors critical for
140 rapid DRW-induced development in such an otherwise unfavorable environment. The
141 paper is organized as follows. An overview of the reanalysis data and the piecewise
142 PV inversion method utilized in this study is detailed in section 2. Section 3 provides
143 a synoptic evolution of the lifecycle of the November 2019 cyclone from 12 hours
144 before genesis to post-occlusion and affirms that this is a DRW-induced development
145 while highlighting its exceptional nature. The evolution of the lifecycle of the storm
146 through the lens of piecewise PV inversion is discussed in section 4. Comparison of
147 this event to the bottom-up development of *Lothar* along with conclusions and
148 suggestions for further analysis are offered in section 5.

149 **2. Data and Methods**

150 *a. Dataset*

151 Wind speed and direction, temperature, geopotential height, relative humidity,
152 and MSLP data for the NV19 storm were extracted on a limited area domain
153 extending from 10°N to 75°N and 180° to 90°W from the ERA5 data set. The analysis
154 employs ERA5 data at 1-hour intervals from 0000 UTC 01 November to 2300 UTC
155 31 December 2019 with a horizontal grid spacing of $0.25^\circ \times 0.25^\circ$ and 19 vertical
156 levels from 1000 hPa to 100 hPa at a vertical grid spacing of 50 hPa. ERA5 data were
157 then regridded to a grid spacing of $1.0^\circ \times 1.0^\circ$ as coarse data with smooth gradients is

158 more amenable to the PV inversion process (Hoskins et al. 1985). ERA5 hourly
159 MSLP and wind data were compared with the 3-hourly Weather Prediction Center
160 and the 6-hourly Ocean Prediction Center Pacific surface observations to confirm
161 their accuracy.

162 *b. Piecewise PV inversion*

163 First envisioned by Rossby (1940), Ertel (1942) expressed the potential
164 vorticity (often referred to as the Ertel PV (EPV)) as

$$EPV = -g (\zeta_\theta + f) \frac{\partial \theta}{\partial p} \quad (1)$$

165 where g is gravitational acceleration, ζ_θ is the isentropic relative vorticity, f is the
166 planetary vorticity, and $\frac{\partial \theta}{\partial p}$ is a static stability term. EPV is conserved for adiabatic,
167 inviscid flow. Information about the atmospheric flow associated with a distribution
168 of EPV can be extracted through the process of PV inversion (Hoskins et al. 1985;
169 Davis and Emanuel 1991). The inversion of a distribution of PV, often done in
170 pressure coordinates to avoid complexities of θ coordinates, requires knowledge of 1)
171 a horizontal and vertical distribution of PV, 2) prescribed boundary conditions on the
172 domain, and 3) a balance condition which relates the mass to the momentum field. It
173 can be particularly enlightening to partition the PV field into discrete pieces each
174 related to different vertical levels and/or physical processes involved in cyclogenesis,
175 a technique known as *piecewise PV inversion* first introduced by Davis and Emanuel
176 (1991, hereafter DE). Such piecewise PV inversion isolates the mass and momentum
177 fields associated with individual pieces of the total anomalous PV, thus enabling
178 investigation of the effect of each piece on the overall circulation tendency and the
179 advection of the other pieces of the PV. The way the PV is partitioned is thus
180 crucially important to both the procurement and the precision of the resulting insights.

181 The DE inversion method assumes hydrostatic balance and that the magnitude
182 of the rotational part of the flow is much larger than that of the divergent part of the
183 flow. Applying these approximations to the divergence equation and equation (1)
184 results in the system of equations, in spherical coordinates, used in the DE piecewise
185 PV inversion:

$$\nabla^2 \Phi = \nabla \cdot (f \nabla \psi) + \frac{2}{a^4 \cos^2 \phi} \frac{\partial \left(\frac{\partial \psi}{\partial \lambda}, \frac{\partial \psi}{\partial \phi} \right)}{\partial (\lambda, \phi)} \quad (2)$$

$$\text{EPV} = \frac{g \kappa \pi}{p} \left[(f + \nabla^2 \psi) \frac{\partial^2 \Phi}{\partial^2 \pi} - \frac{1}{a^2 \cos^2 \phi} \frac{\partial^2 \psi}{\partial \lambda \partial \pi} \frac{\partial^2 \Phi}{\partial \lambda \partial \pi} - \frac{1}{a^2} \frac{\partial^2 \psi}{\partial \phi \partial \pi} \frac{\partial^2 \Phi}{\partial \phi \partial \pi} \right], \quad (3)$$

186 where Φ is the geopotential, ψ is the nondivergent streamfunction, ϕ is the latitude, λ
 187 is the longitude, a is the radius of the earth, p is the pressure, $\kappa = R/c_p$, and π is the
 188 Exner function $\left[c_p \left(\frac{p}{p_0} \right)^\kappa \right]$, which serves as the vertical coordinate (DE). Equation (2),
 189 the nonlinear balance condition of Charney (1955), relates the wind and pressure
 190 fields according to the assumption that the rotational part of the flow is much larger
 191 than the divergent part of the flow, which has been shown to be a good approximation
 192 to observed atmospheric flows, especially for flows of the synoptic scale (e.g., Davis
 193 et al. 1996). The unbalanced portion of the flow corresponds primarily to the
 194 nondivergent component of the ageostrophic wind and cannot be recovered using PV
 195 inversion techniques (Davis et al. 1996). The nondivergent flow field recovered from
 196 piecewise PV inversion was compared to the pure ERA5 flow field across a
 197 $10^\circ \times 10^\circ$ box centered on the NV19 MSLP minimum. Differences between these
 198 two flow fields did not exceed 20% for 950 hPa, 10% for 900 hPa, and 5% at and
 199 above 850 hPa meaning that piecewise PV inversion is accurately representing this
 200 development throughout the troposphere. These larger differences near the surface are
 201 directly attributed to stronger nondivergent ageostrophic components of the wind in
 202 the vicinity of the intense NV19 cyclone.

203 Piecewise PV inversion is accomplished by first performing an inversion on
 204 the full perturbation PV which is defined by subtracting the 2-month mean PV from
 205 the instantaneous PV at 1-hour increments at each grid point during the development
 206 of the NV19 storm. For the full perturbation PV inversion, equations (2) and (3) are
 207 solved simultaneously for the hourly Φ and ψ , with the lateral boundary conditions
 208 for Φ and ψ prescribed by subtracting the 2-month mean Φ and ψ from the
 209 instantaneous ERA5 data. The boundary ψ was initialized using Neumann boundary
 210 conditions such that the component of the total wind from the ERA5 data which was
 211 perpendicular to the boundary was equivalent to the gradient of ψ along that same

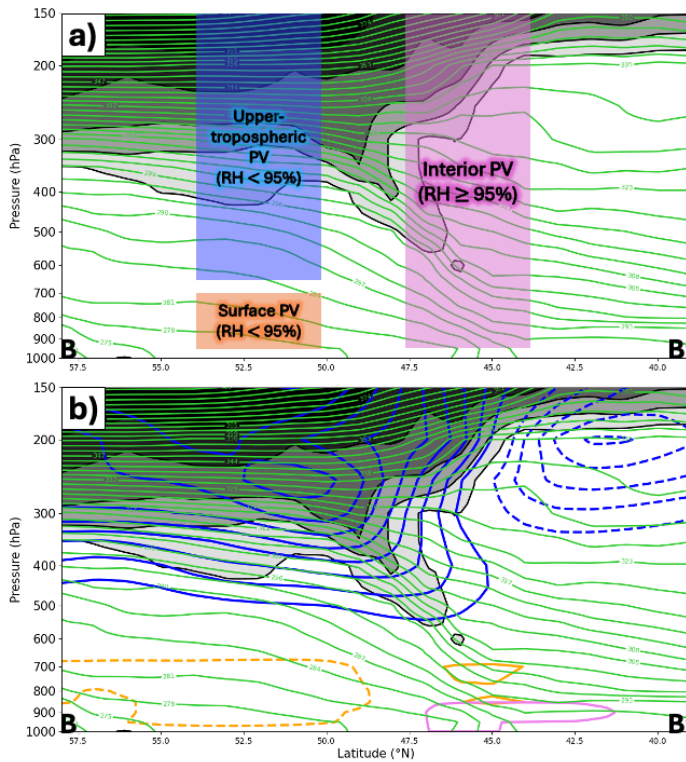
212 boundary, and that the net divergence out of the domain was zero. Neumann boundary
213 conditions consistent with hydrostatic balance were prescribed along the bottom (top)
214 of the domain such that the vertically-averaged perturbation potential temperature,
215 defined following the same method used in calculating the perturbation PV, between
216 1000 hPa and 950 hPa (150 hPa and 100 hPa) were used to define Φ and ψ along the
217 bottom (top) of the domain. Full static PV inversion was performed across the entire
218 horizontal and vertical domain and, to assure a stable solution of equations (2) and
219 (3), negative PV values were manually adjusted to a small positive constant of 0.01
220 PVU (where $1 \text{ PVU} = 1 \times 10^{-6} \text{ m}^2 \text{ s}^{-1} \text{ K kg}^{-1}$) and the static stability was required to
221 remain positive throughout the domain. The threshold for convergence was set to 0.1
222 meter, the over-relaxation parameters for Φ and ψ were 1.8 and 1.9, respectively, and
223 the under-relaxation parameter was set to 0.3. Each hourly time-step reached
224 convergence after approximately 150 iterations. The reader is referred to DE for a
225 complete description of the boundary conditions and numerical methods used to solve
226 this system.

227 *c. Partitioning method*

228 The next step in performing piecewise PV inversion is to partition the full
229 perturbation PV field into three distinct pieces. Here we follow a modified version of
230 the piecewise partitioning described in Davis (1992), Korner and Martin (2000), and
231 Winters and Martin (2017) which employs both isobaric and relative humidity
232 criteria. Both the partitioning, and the consequent analysis, were found to be
233 insensitive to a robust, but physically reasonable range of choices considered for the
234 RH threshold (not shown).

235 The three-way partitioning method used in this study is depicted in Figure 1.
236 The surface PV (SFC) is defined as perturbation PV between 950 hPa and 700 hPa in
237 air with a relative humidity $< 95\%$, and also includes the perturbation potential
238 temperature on the bottom boundary of the domain. SFC is designed to represent the
239 influence of near-surface potential temperature perturbations on the flow throughout
240 the domain, as these are equivalent to PV perturbations along the bottom boundary
241 (Bretherton 1966). The interior PV (INT) is defined as the perturbation PV between

242 950 hPa and 150 hPa found in air with a relative humidity $\geq 95\%$. INT is designed to
 243 represent the influence of diabatic generation and erosion of PV associated with latent
 244 heat release, a process central to DRW propagation (Boettcher and Wernli 2013;
 245 Terpstra et al. 2015; Tamarin and Kaspi 2016; Kohl and O’Gorman 2022). Therefore,
 246 INT can be considered a residual representing both the influence of diabatic processes
 247 and other remnant PV anomalies. The upper-tropospheric PV (UPTROP) is defined as
 248 the perturbation PV between 650 hPa and 150 hPa found in air with a relative
 249 humidity $< 95\%$ and includes the perturbation potential temperature on the top
 250 boundary of the domain. UPTROP is designed to isolate the role of dry middle- and
 251 upper-tropospheric, and stratospheric PV intrusions on the flow, along with
 252 stratospheric potential temperature anomalies.



253
 254 Fig. 1. Schematic of the piecewise partitioning scheme used in the inversion of the perturbation
 255 PV overlaid on a cross section along B-B’ in Fig. 4e. Solid, green contours are potential
 256 temperature contoured every 3 K starting at 300 K. Potential vorticity is shaded in gray every 2
 257 PVU ($1 \text{ PVU} = 1 \times 10^{-6} \text{ m}^2 \text{ s}^{-1} \text{ K kg}^{-1}$) starting at 2 PVU. Labeled boxes correspond to the three
 258 distinct pieces of the total perturbation PV with the top and bottom boundaries of each box
 259 indicating the isobaric layers included within those pieces. Criterion for relative humidity used to
 260 distinguish the pieces of PV are as indicated. (b) As in (a), but with the distribution of upper-

261 tropospheric perturbation PV (blue contours), interior perturbation PV (pink contours), and
 262 surface perturbation PV (orange contours) at 1200 UTC 26 November 2019 contoured every 0.5
 263 PVU . Positive (negative) perturbation PV anomalies denoted by the solid (dashed) contours.
 264

265 Static inversion is performed for the SFC and UPTROP PV as for the full
 266 perturbation PV, but with Φ and ψ on the horizontal boundaries being set to zero.
 267 Inversion of the INT PV is not performed; rather, its associated Φ and ψ (Φ_{INT} and
 268 ψ_{INT} , respectively) are presented as:

$$\Phi_{INT} = \Phi_{FULL\ PERT} - (\Phi_{SFC} + \Phi_{UPTROP}) \quad (4)$$

269 and

$$\psi_{INT} = \psi_{FULL\ PERT} - (\psi_{SFC} + \psi_{UPTROP}) \quad (5)$$

270 where Φ_{INT} and ψ_{INT} on the horizontal boundaries are set equal to the full
 271 perturbation Φ and ψ , not zero. The decision to prescribe these results was motivated
 272 by numerous unsuccessful trials in which the static inversion of the INT PV, though
 273 reaching convergence, consistently returned unphysical results. Similar unphysical
 274 results are detailed in both Ahmadi-Givi et al. (2004) and Bracegirdle and Gray
 275 (2009). Those studies concluded that such results derive from a breakdown of the
 276 Charney nonlinear balance condition (Charney 1955) in regions where strong
 277 divergence becomes collocated with regions of strong diabatic heating. The
 278 development of the NV19 DRW was strongly influenced by diabatic heating
 279 collocated with the lower-tropospheric vortex, hence, the governing physics were well
 280 outside the requisite nonlinear balance in equation (2). In such situations, convergence
 281 to a solution for the INT PV, characterized by heavy diabatic modification for
 282 extended periods of time, will produce a result in which the wind field is not
 283 dynamically consistent with the pressure field and the DE system of equations for
 284 piecewise PV inversion will no longer be valid. As the present analysis seeks to
 285 isolate the influence of the INT PV on aspects of the development, calculating it as a
 286 residual affords a tenable means to that end given the circumstances. This residual
 287 also predominantly corresponds to moist diabatic processes, as the influences of
 288 radiation and turbulence on the PV are much smaller in magnitude on the timescales
 289 considered.

290 3. Synoptic Evolution and Anomalous Nature

291 a. Overview

292 We use hourly data from the ERA5 (Hersbach et al. 2020) to describe the synoptic
293 overview of the NV19 storm and will focus on twelve hour increments from 1200
294 UTC 25 November 2019, prior to the nascent stage of development, to 0000 UTC 27
295 November 2019, past the period of its most rapid development and as the storm made
296 landfall on the West Coast of the United States.

297 1) 1200 UTC 25 November 2019

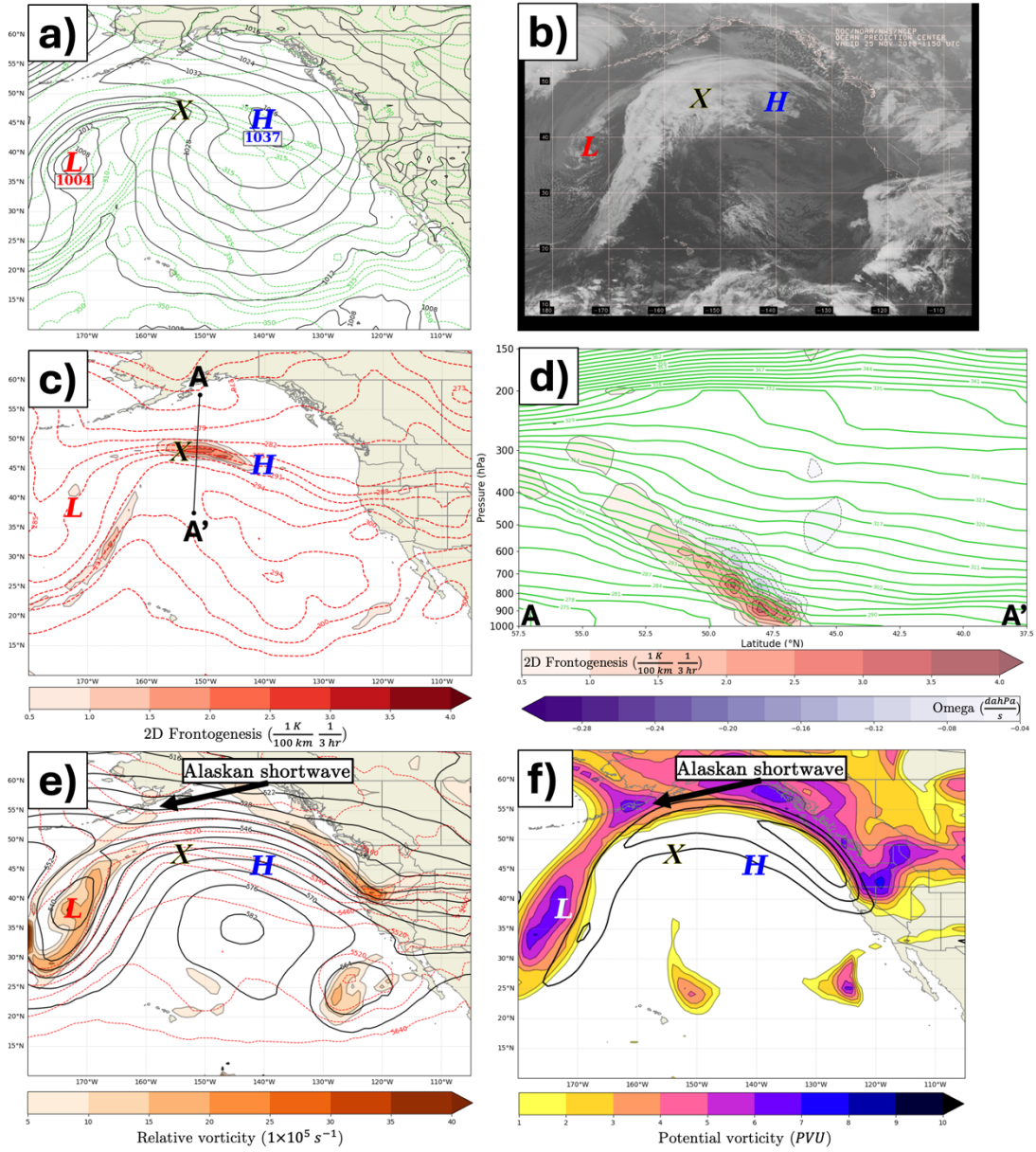
298 Twelve hours before the NV19 storm developed its own closed circulation at sea-
299 level, a predominantly zonally-oriented surface baroclinic zone, indicated by a strong
300 gradient of 950 hPa equivalent potential temperature (θ_e) contours, was draped
301 southeastward from an almost cutoff low pressure system to the west through the
302 center of a strong surface anticyclone to the east (Fig. 2a). Though there was no
303 closed isobar evident at this time, there was a 950 hPa relative vorticity maximum
304 (yellow-highlighted “X”) at the intersection of this baroclinic zone with a more
305 meridionally oriented cold frontal baroclinic zone (Figs. 2a,b). The same baroclinic
306 zones were reflected in the isentropes at 850 hPa, with strong positive frontogenesis
307 occurring due east of the 950 hPa vorticity maximum along the warm front (Fig. 2c).
308 Positive 2D frontogenesis, calculated using

$$\mathfrak{F}_{2D} = \frac{1}{|\nabla\theta|} \left[\left(\frac{\partial\theta}{\partial x} \right) \left(-\frac{\partial\vec{V}}{\partial x} \cdot \nabla\theta \right) + \left(\frac{\partial\theta}{\partial y} \right) \left(-\frac{\partial\vec{V}}{\partial y} \cdot \nabla\theta \right) \right], \quad (6)$$

309

310 was maximized between 850 and 900 hPa along the baroclinic zone on which the
311 cyclone developed, with negative omega (ascent) focused on the warm side of a deep
312 baroclinic zone in response to that frontogenesis (Fig. 2d). At 500 hPa, the surface
313 development region was downstream of the nearly cutoff low pressure center to the
314 southwest and a shortwave feature to the northwest over the Alaska Peninsula (Fig.
315 2e). The surface development region was centered in the right entrance region of a
316 downstream, anticyclonically-curved jet streak at 300 hPa characterized by weak

317 along-flow acceleration in the entrance region (Fig. 2f). A 300 hPa PV maximum over
 318 the Aleutians was the tropopause-level counterpart to the shortwave at 500 hPa (Figs.
 319 2e,f).



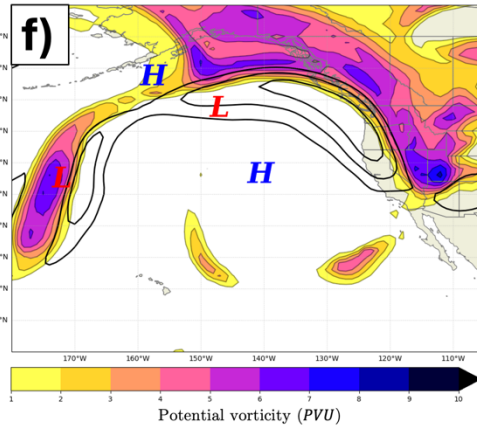
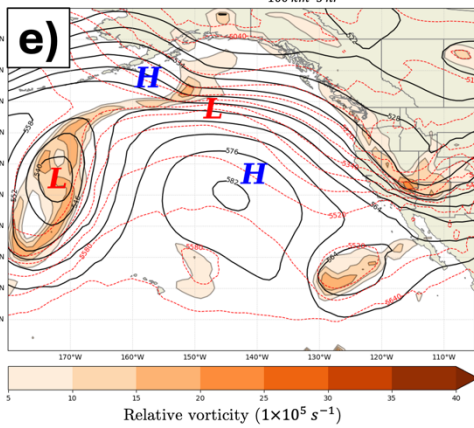
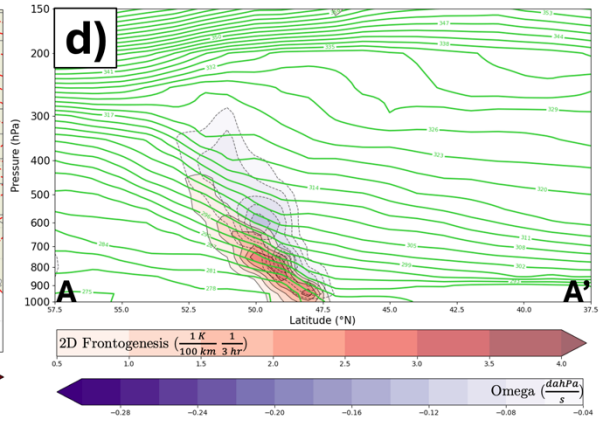
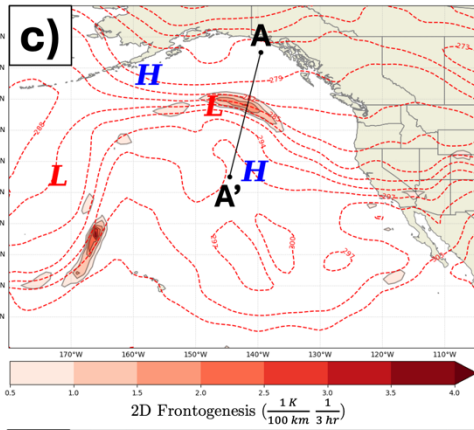
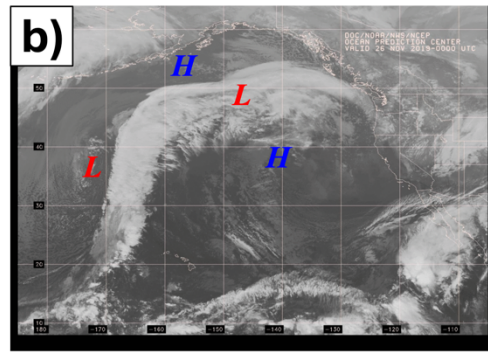
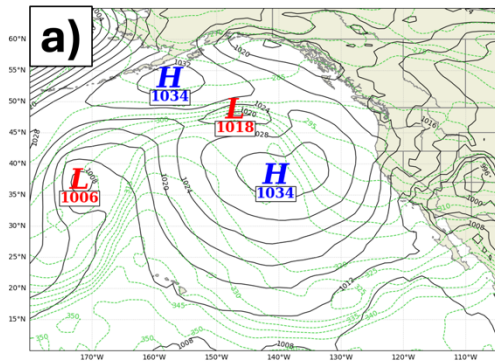
320

321 Fig. 2. (a) Sea-level pressure and 950 hPa equivalent potential temperature (θ_e) from the ERA5
322 reanalysis valid at 1200 UTC 25 November 2019. Solid, black lines are isobars contoured every 4
323 hPa. Dashed, green lines are 950 hPa moist isentropes contoured every 5 K. “H” denotes the
324 centers of high pressure systems whereas “L” denotes centers of low pressure systems. “X”
325 denotes the development region of NV19 storm. (b) GOES-17 infrared imagery of the northeast
326 Pacific basin valid at 1150 UTC 25 November 2019. “H”, “L”, and “X” as in panel (a). (c)
327 Potential temperature and positive horizontal frontogenesis at 850 hPa from the ERA5 reanalysis
328 valid at 1200 UTC 25 November 2019. Dashed, red contours are isentropes contoured every 3 K.
329 Shading indicates positive frontogenesis function values shaded every $0.5 \text{ K (100km)}^{-1} (3\text{hr})^{-1}$
330 starting at $0.5 \text{ K (100km)}^{-1} (3\text{hr})^{-1}$. “H”, “L”, and “X” as in panel (a). Black line indicates the cross
331 section shown in panel (d). (d) Cross section along A-A’ in panel (c) of potential temperature,
332 frontogenesis, and negative omega valid at 1200 UTC 25 November 2019. Potential temperature
333 (green) contoured every 3 K starting at 300 K. Positive frontogenesis function (red shading)
334 shaded every $0.5 \text{ K (100km)}^{-1} (3\text{hr})^{-1}$. Negative omega (purple dashed shading) shaded every
335 $-0.04 \text{ daPa s}^{-1}$ starting at $-0.04 \text{ daPa s}^{-1}$. (e) 1000 hPa – 500 hPa thickness and relative vorticity
336 at 500 hPa from the ERA5 reanalysis valid at 1200 UTC 25 November 2019. Red dashed contours
337 are lines of constant thickness contoured every 60 meters. Shading indicates positive relative
338 vorticity shaded every $5 \times 10^{-5} \text{ s}^{-1}$ starting at $5 \times 10^{-5} \text{ s}^{-1}$. “H”, “L”, and “X” as in panel (a).
339 (f) Potential vorticity and wind speed at 300 hPa from the ERA5 reanalysis valid at 1200 UTC 25
340 November 2019. Solid, black contours are wind speeds contoured every 10 m s^{-1} starting at 50 m
341 s^{-1} . Shading indicates potential vorticity at 300 hPa shaded every 0.5 PVU ($1 \text{ PVU} = 1 \times 10^{-6} \text{ m}^2$
342 $\text{s}^{-1} \text{ K kg}^{-1}$) starting at 0.5 PVU. “H”, “L”, and “X” as in panel (a). “L” denoting the low pressure
343 system changed to light blue for visibility.

344 2) 0000 UTC 26 November 2019

345 By 0000 UTC 26 November 2019, a weak surface cyclone was discernable along
346 the baroclinic zone that stretched zonally through the anticyclone (Fig. 3a). This
347 disturbance had begun to develop its own separate cloud feature by this time (Fig. 3b).
348 The 850 hPa baroclinic zone and positive frontogenesis maintained its previous
349 spatial relationship with the developing surface cyclone (Fig. 3c), with frontogenesis
350 located to the east and northeast of the surface cyclone along the developing warm
351 front. Positive frontogenesis was now maximized at 800 hPa as the frontal slope
352 notably steepened from the previous time (compare Fig. 2d to Fig. 3d). In response to
353 this evolution, the ascent associated with the lower-tropospheric frontogenesis was

354 deeper. The shortwave feature at 500 hPa began to strengthen to the northwest of the
355 surface cyclone, indicated by the increase in positive relative vorticity along the
356 shortwave axis (Fig. 3e). The proximity of this shortwave resulted in a region of
357 cyclonic vorticity advection (CVA) by the thermal wind, indicative of column mean
358 divergence and ascent (Sutcliffe 1947), coincident with the surface cyclone at this
359 time. At 300 hPa, the surface cyclone maintained its position relative to the right
360 entrance region of the downstream, anticyclonically-curved jet streak with now
361 stronger along-flow speed change characterizing the entrance region (Fig. 3f). The
362 shortwave feature at 300 hPa had also strengthened as indicated by the expanding
363 region of large 300 hPa positive PV to the north-northwest of the surface cyclone
364 (Fig. 3f).



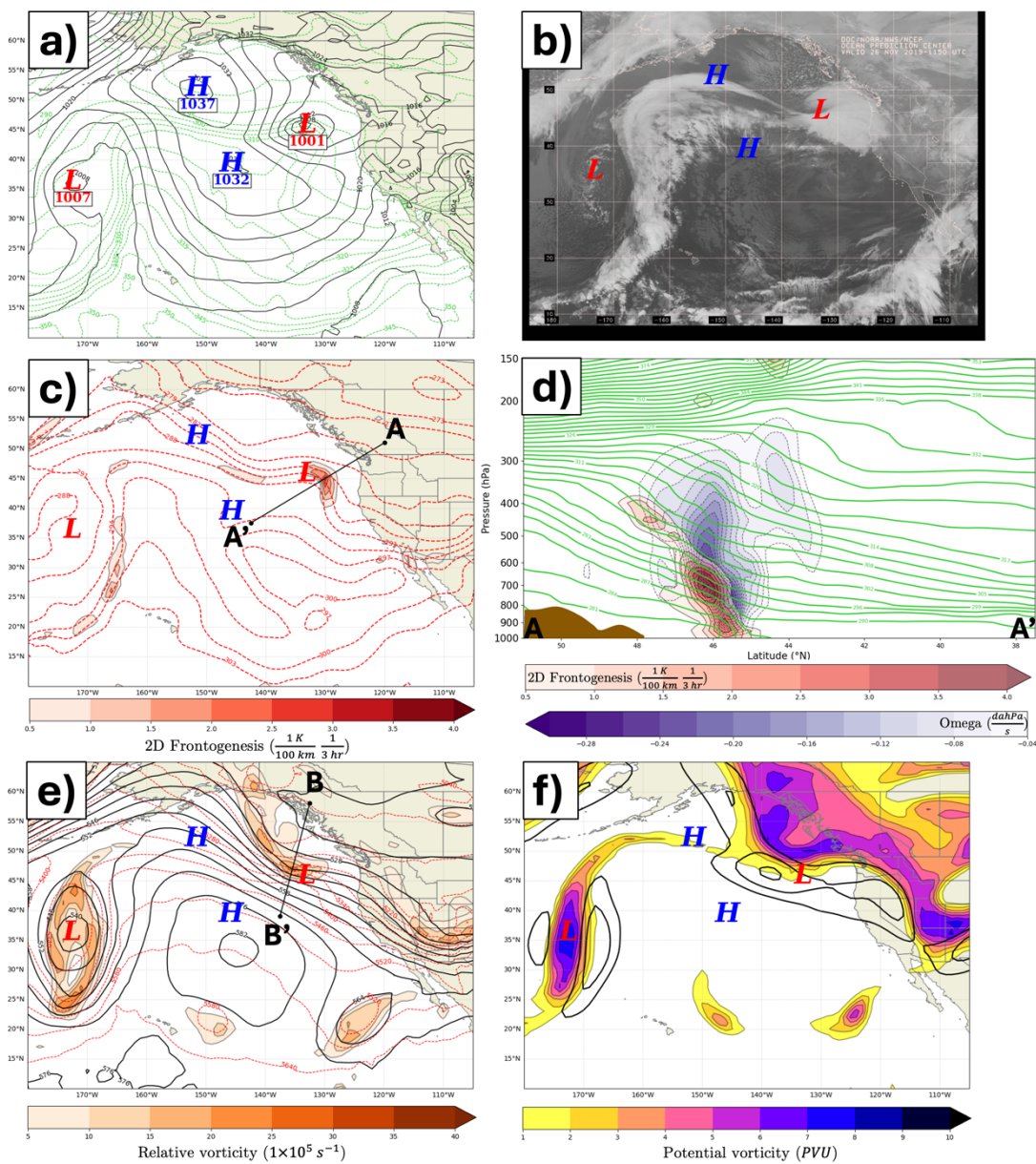
365

366 Fig. 3. (a) As in Fig. 2a except for 0000 UTC 26 November 2019. (b) As in Fig. 2b except for
367 0000 UTC 26 November 2019. (c) As in Fig. 2c except for 0000 UTC 26 November 2019. (d) As
368 in Fig. 2d except for 0000 UTC 26 November 2019. (e) As in Fig. 2e except for 0000 UTC 26
369 November 2019. (f) As in Fig. 2f except for 0000 UTC 26 November 2019.

370 3) 1200 UTC 26 November 2019

371 Twelve hours after initial development (Fig. 4a), the NV19 storm completely
372 bisected the anticyclone within which it initially developed (see Fig. 3a). Well-
373 defined cold and warm fronts now characterized the cyclone, as shown by the 950 hPa
374 θ_e , with pressure troughs associated with both fronts. At this time, the storm was
375 beginning its twelve-hour period of most rapid deepening as it approached the
376 California-Oregon border. The storm was also beginning to transition from a
377 baroclinic leaf (R. B. Weldon 1979) to a more classic comma shape (Fig. 4b). The
378 primary band of positive frontogenesis at 850 hPa remained robust and associated
379 with the surface warm front while a band of weaker, positive frontogenesis developed
380 along the cold front (Fig. 4c). The cyclone center was now clearly located at the apex
381 of the 850 hPa thermal ridge. Positive frontogenesis peaked at 700 hPa as the warm
382 front neared its maximum strength and the associated ascent expanded and intensified
383 throughout the depth of the mid- to lower-troposphere, now being maximized around
384 750 hPa (Fig. 4d). Rapid intensification and elongation of the 500 hPa positive
385 vorticity feature occurred to the west-northwest of the surface cyclone, coincident
386 with a sharp temperature gradient, indicative of the development of a potent upper-
387 level jet/front system (Fig. 4e). This intensification focused vigorous CVA by the
388 thermal wind directly above the surface cyclone and, consequently, the central
389 pressure of the NV19 storm began to rapidly drop. The trough in the 1000-500 hPa
390 thickness also lagged the geopotential height trough resulting in along-flow cold air
391 advection coincident with the 500 hPa relative vorticity maximum (Fig. 4e). The
392 thermal gradient directly west of the cyclone had intensified within this same twelve-
393 hour interval. The region of increased baroclinicity was reflected in an increase in
394 wind speed at 300 hPa, at the base of the shortwave feature (Fig. 4f). This wind speed
395 intensification also situated the NV19 storm in the left exit region of a newly formed
396 jet streak tied to the development of the upper-level jet/front system (e.g. Shapiro

397 1981, 1983; Lackmann et al. 1997; Martin 2014), providing another mechanism for
 398 enhancing upper-tropospheric mass evacuation and lower-tropospheric cyclogenesis.

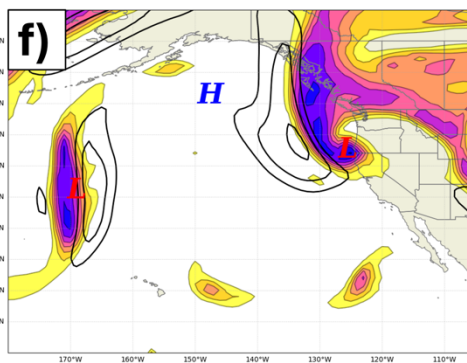
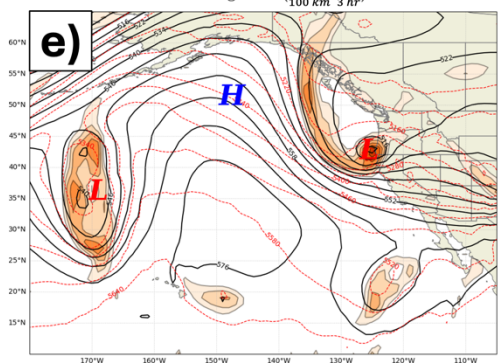
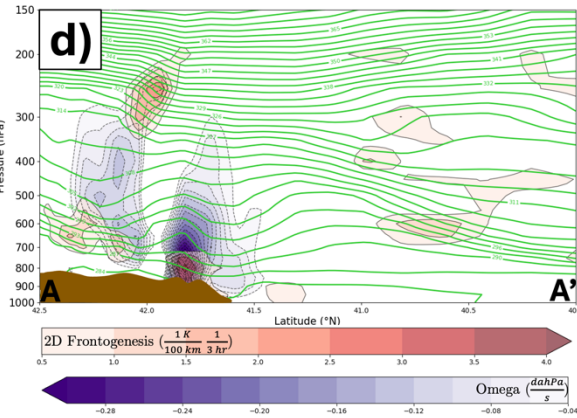
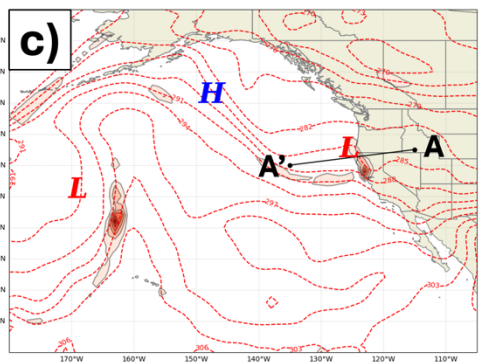
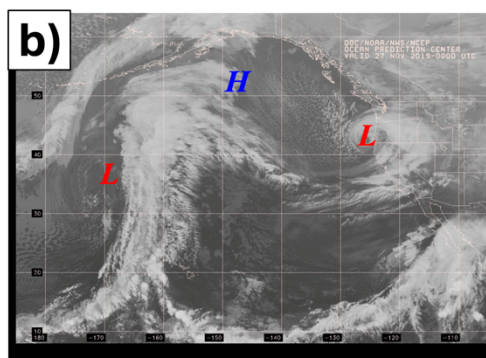
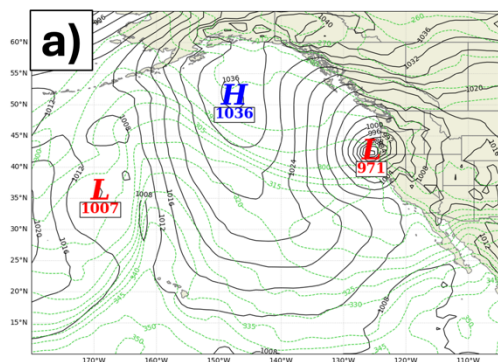


399

400 Fig. 4. (a) As in Fig. 3a except for 1200 UTC 26 November 2019. (b) As in Fig. 3b except for
401 1150 UTC 26 November 2019. (c) As in Fig. 3c except for 1200 UTC 26 November 2019. (d) As
402 in Fig. 3d except for 1200 UTC 26 November 2019. (e) As in Fig. 3e except for 1200 UTC 26
403 November 2019. (f) As in Fig. 3f except for 1200 UTC 26 November 2019.

404 4) 0000 UTC 27 November 2019

405 In the twenty-four hours after initial development, the storm had deepened a total
406 of 47 hPa to a central MSLP of 971 hPa, well exceeding the definition of explosive
407 cyclogenesis first defined in Sanders and Gyakum (1980) (Fig. 5a). In fact, the storm
408 had deepened from 1020 hPa at 2200 UTC 25 November to 971 hPa at 2200 UTC 26
409 November, resulting in a maximum 24-hour deepening rate of 49 hPa. At 0000 UTC
410 27 November, the NV19 storm was just a few hours from making landfall on the west
411 coast of the United States near Crescent City, California (Figs. 5a,b). The intense
412 pressure gradient to the south of the cyclone center resulted in surface winds greater
413 than 45 m s^{-1} near the California-Oregon border and 24 m waves off the California
414 coast (094 Cape Mendocino buoy). By this time, the positive frontogenesis at 850 hPa
415 associated with the warm front was undoubtedly influenced by the steep topography
416 adjacent to the United States West Coast (Fig. 5c,d) as the frontal structure had clearly
417 weakened (Fig. 5d). Lower-tropospheric ascent at this time reached its largest values
418 of the cyclone lifecycle, also undoubtedly influenced by the steep topography. A well-
419 developed trough with substantial CVA by the thermal wind and an elongated
420 streamer of vorticity at 500 hPa were both still forcing ascent in and around the
421 surface cyclone (Fig. 5e), with the strongest CVA by the thermal wind situated south
422 of the cyclone (not shown). The intensified vortex strip was a manifestation of the
423 continued development of the associated upper-level jet/front system (Fig. 5e). The jet
424 streak to the west of the surface cyclone increased in intensity and the surface cyclone
425 remained in the left exit region as the jet raced southeastward on the upstream side of
426 a newly carved out upper trough (Fig. 5f). The surface cyclone was now vertically
427 stacked as the 300 hPa PV and 500 hPa vorticity were all maximized at the same
428 location directly above the surface cyclone (Fig. 5e,f).



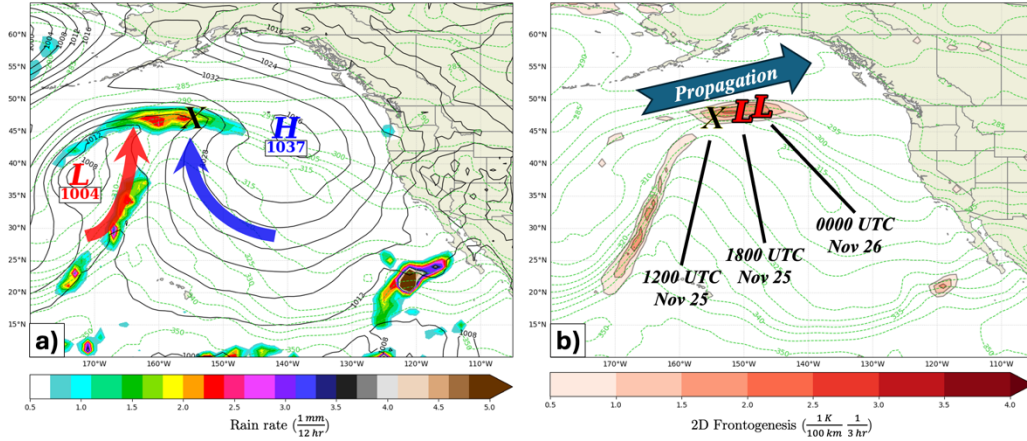
429

430 Fig. 5. (a) As in Fig. 4a except for 0000 UTC 27 November 2019. (b) As in Fig. 4b except for
431 0000 UTC 27 November 2019. (c) As in Fig. 4c except for 0000 UTC 27 November 2019. (d) As
432 in Fig. 4d except for 0000 UTC 27 November 2019. (e) As in Fig. 4e except for 0000 UTC 27
433 November 2019. (f) As in Fig. 4f except for 0000 UTC 27 November 2019.

434 *b. The NV19 cyclone as a Diabatic Rossby wave*

435 As first introduced by Raymond and Jiang (1990), Snyder and Lindzen (1991),
436 and Parker and Thorpe (1995) and first classified by Moore and Montgomery (2004,
437 2005), a DRW is a lower-tropospheric vortex borne of positive PV production in the
438 vicinity of a lower-tropospheric baroclinic zone that is situated below mid-
439 tropospheric latent heat release. During the early development phase of the NV19
440 storm, a nearly cutoff low pressure system south of the Aleutian Islands and an
441 expansive high pressure system off the coast of the Pacific Northwest conspired to
442 produce southerly flow which overan a predominantly zonal baroclinic zone
443 stretching across the northeast Pacific Ocean at 1200 UTC 25 November 2019 (Fig.
444 6a). This flow induced strong lower-tropospheric frontogenesis which, in turn,
445 spawned the production of precipitation along the baroclinic zone as indicated by the
446 12-hour rainfall rates from the ERA5 data. The ERA5 12-hour rainfall rates agreed
447 with 24-hour rainfall rates from the Integrated Multi-satellitE Retrievals for the
448 Global Precipitation Measurement (GPM) mission (IMERG) in terms of spatial
449 distribution and location of maxima (not shown). A lower-tropospheric circulation
450 developed as a result of the latent heat release that accompanied the production of
451 precipitation. This circulation then propagated along the baroclinic zone for at least
452 the next 12 hours as shown by the location of the SLP minimum along the mean 950
453 hPa θ_e gradient averaged between 1200 UTC 25 November and 0000 UTC 26
454 November 2019 (Fig. 6b). Thus, there was strong frontogenesis and moist ascent
455 along the baroclinic zone (Figs. 2c,d and 3c,d) driving precipitation development and
456 latent heat release which, in turn, mobilized lower-tropospheric diabatic PV
457 “production” (Fig. 6a,b). The resulting diabatically-generated vortex provided
458 differential temperature advection near the surface which then propagated the DRW
459 vortex. Propagation speeds averaged 24.4 m s^{-1} throughout the entire DRW lifecycle
460 with a maximum 1-hourly propagation speed of 47.6 m s^{-1} between 1200 UTC and

461 1300 UTC 26 November. This average far exceeded the threshold of 11.6 m s^{-1} for
 462 DRW propagation established in Boettcher and Wernli (2013) and neared the rapid
 463 average propagation speeds of $\sim 30 \text{ m s}^{-1}$ associated with *Lothar* (Wernli et al. 2002).



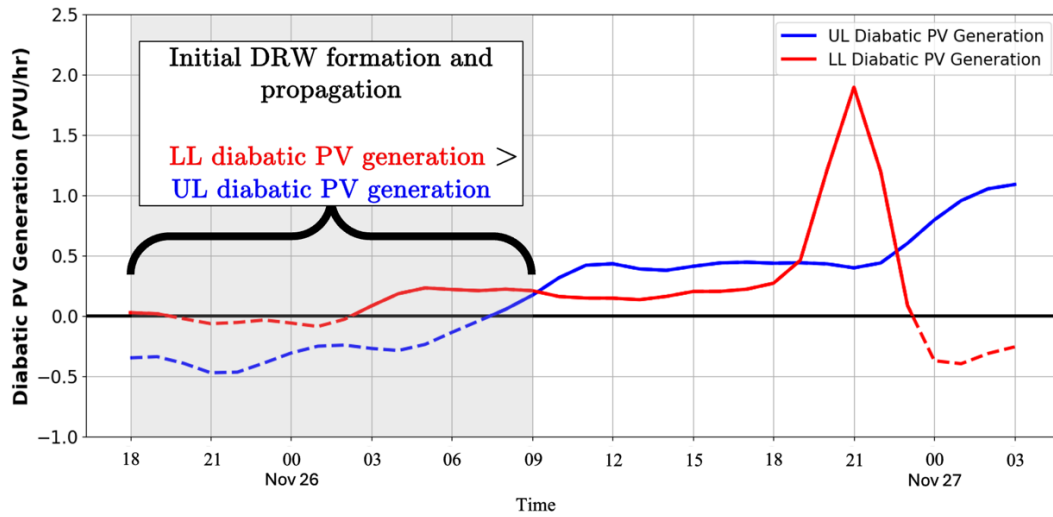
464
 465 Fig. 6. (a) Sea-level pressure and 950 hPa equivalent potential temperature (θ_e) from the ERA5
 466 reanalysis valid at 1200 UTC 25 November 2019. Solid, black lines are isobars contoured every 4
 467 hPa. Dashed, green lines are 950 hPa moist isentropes contoured every 5 K. Shading indicates the
 468 rainfall rate valid at 1800 UTC 25 November 2019 shaded every $0.25 \text{ mm } 12\text{hr}^{-1}$ starting at 0.5
 469 $\text{mm } 12\text{hr}^{-1}$. “H” denotes the center of the high pressure system whereas “L” denotes the centers of
 470 the low pressure systems. “X” denotes the development region of NV19 storm. Red and blue
 471 annotated arrows indicate the lower-tropospheric synoptic-scale flow. (b) Propagation of sea-level
 472 pressure minima along the 12-hour mean 950 hPa θ_e between 1200 UTC 25 November and 0000
 473 UTC 26 November 2019, as indicated by arrow. Shading indicates the 12-hour mean 950 hPa
 474 positive horizontal frontogenesis between 1200 UTC 25 November and 0000 UTC 26 November
 475 2019 shaded every $0.5 \text{ K } (100\text{km})^{-1} (3\text{hr})^{-1}$. Moist isentropes contoured as in (a). “L” and “X” as
 476 in panel (a).

477
 478 Lastly, the diabatic PV generation rate was assessed according to Eq. (74a) in
 479 Hoskins et al. (1985):

$$480 \quad \dot{Q}_{diab} = Q \frac{\partial \dot{\theta}}{\partial p} \left(\frac{\partial \theta}{\partial p} \right)^{-1} - \dot{\theta} \frac{\partial Q}{\partial p} \left(\frac{\partial \theta}{\partial p} \right)^{-1} \quad (7)$$

481 where Q is the potential vorticity, θ is the potential temperature, and $\dot{\theta}$ is the potential
 482 temperature tendency. Diabatic PV generation rate was averaged over two layers of
 483 near equal height following Kohl and O’Gorman (2022) and across a $10^\circ \times 10^\circ$ box

484 centered on the NV19 MSLP minimum throughout its evolution. The average rate of
 485 diabatic PV generation in the lower-layer, 950 hPa to 550 hPa, (upper-layer, 500 hPa
 486 to 150 hPa,) was zero (negative) as the DRW formed from 1800 UTC 25 November
 487 to 0000 UTC 26 November, and then positive (remained negative) as the NV19 DRW
 488 strengthened and propagated eastward from 0000 UTC to 0900 UTC 26 November
 489 (Fig. 7). The positive PV anomaly in the lower-layer, the NV19 DRW, and the
 490 negative PV anomaly in the upper-layer were both growing through the diabatic
 491 generation of PV as DRW propagation and strengthening began, which agrees with
 492 the DRW growth mode presented in Kohl and O’Gorman (2022) and adds additional
 493 support to the notion that the NV19 storm originated as a DRW.



494
 495 Fig. 7. The layer-averaged diabatic PV generation rate in PVU hr⁻¹ (1 PVU = 1 × 10⁻⁶ m² s⁻¹ K
 496 kg⁻¹) for the upper-layer (500 hPa to 150 hPa, ‘UL’) and the lower-layer (950 hPa to 550 hPa,
 497 ‘LL’) from 1800 UTC 25 November to 0300 UTC 27 November 2019 averaged across a
 498 10° × 10° box centered on the NV19 storm. Diabatic PV generation rate is contoured in solid
 499 blue for the upper-layer and solid red for the lower-layer with negative diabatic PV generation
 500 rates for both layers represented as dashed contours.

501 *c. The anomalous nature of the NV19 storm*

502 Northwestly flow cyclogenesis events over the northeast Pacific Ocean are
 503 common and well-documented (Reed and Albright 1986; Yoshiike and Kawamura
 504 2009; Lang and Martin 2012; Iwao et al. 2012; Iizuka et al. 2013) along with
 505 explosive cyclogenesis (EC) events over this part of the Pacific Ocean (Roebber 1984;

506 Wang and Rogers 2001; Boettcher and Wernli 2013; Zhang et al. 2017). Despite the
507 relative frequency of EC events over the northeastern Pacific Ocean, the storm track,
508 deepening rate, and location of maximum deepening for the NV19 storm were all well
509 outside of established climatologies for this part of the world.

510 First, the NV19 storm had an unusual track. Roebber (1984) constructed a
511 climatology of Northern Hemisphere EC events over the period from 1976 to 1982
512 while Wang and Rogers (2001) compiled a similar climatology for the period from
513 1985 to 1996. In still another climatology (from 2000 to 2015), Zhang et al. (2017)
514 specifically focused on EC events over the northern Pacific Ocean. All three studies
515 highlighted preferred regions for periodic EC events: off the east coast of Japan, off
516 the east coast of the United States, and in the central Gulf of Alaska. After genesis, a
517 majority of the cyclones track southwest to northeast based on the roughly 30-year
518 period covered by the three, non-consecutive climatologies. Tamarin and Kaspi
519 (2016) noted that the predominant region of latent heat release associated with DRWs
520 typically occurs to the northeast of the DRW center, which propagates the DRW
521 eastward and poleward. The NV19 cyclone also initially formed in the central Gulf of
522 Alaska and tracked nearly due east before beginning a northwest to southeast track
523 (Figs. 2-5). Zhang et al. (2017) divided their database of EC storm tracks into separate
524 regions of the northern Pacific in which clustering of cyclogenesis events occurred.
525 The storm track of the NV19 cyclone was rotated approximately 90° to the right of
526 both the northeastern Pacific Ocean EC storm tracks from the Zhang et al. (2017)
527 climatology (their Fig. 5e) and the typical direction of DRW propagation from
528 Tamarin and Kaspi (2016). The NV19 track was also mainly outside of the storm
529 track densities presented in Roebber (1984), Wang and Rogers (2001), and Zhang et
530 al. (2017). Thus, the storm track associated with the NV19 storm was unusual based
531 on at least 30 years of non-consecutive climatologies presented in the literature.

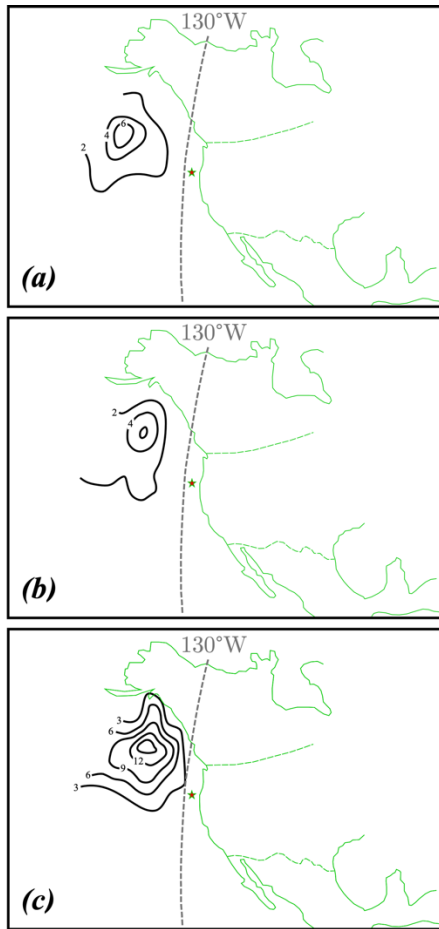
532 Second, the deepening rate of EC events has been quantified using the "Bergeron"
533 since it was originally defined by Sanders and Gyakum (1980) as

534

$$1 \text{ Bergeron} = \frac{24 \text{ hPa}}{24 \text{ hours}} \cdot \frac{\sin(\phi)}{\sin(60^\circ)} \quad (8)$$

535 where ϕ is the latitude of the cyclone center normalized to 60°N. A cyclogenesis
536 event must accomplish a deepening rate equivalent to at least 1 Bergeron to be
537 classified as explosive. Roebber (1984) and Zhang et al. (2017) used normalized
538 latitudes of 42.5° and 45°, respectively, in the denominator of (8) as these mean
539 latitudes were more representative of the mean latitude of explosive cyclogenesis
540 events presented in their studies. The deepening rate of the NV19 storm using the
541 Roebber (1984) and the Zhang et al. (2017) definitions was 2.14 Bergerons and 2.04
542 Bergerons, respectively. This deepening rate ranks the NV19 storm in the 99th
543 percentile when focusing on the 115 EC cases over the northern Pacific Ocean from
544 the Roebber (1984) climatology and in the 93rd percentile when focusing on the 120
545 EC cases over the northeast Pacific region from the Zhang et al. (2017) climatology.
546 Further, the maximum 6-hour deepening rate of 22 hPa between 1200 UTC to 1800
547 UTC 26 November 2019 rivals that of the maximum 6-hour deepening rate of 26 hPa
548 accomplished by the *Braer* storm, the strongest extratropical cyclone on record based
549 both on minimum SLP and deepening rate (Lim and Simmonds 2002; Odell et al.
550 2013). Therefore, the maximum 6-hour deepening rate of the NV19 storm was among
551 the strongest ever recorded for all extratropical cyclones in the Pacific and Atlantic
552 Ocean basins.

553 Finally, frequency contours of northern Pacific Ocean EC events are provided
554 using the Roebber (1984), Wang and Rogers (2001), and Zhang et al. (2017)
555 climatologies (Fig. 8). The furthest eastward extent of any of these frequency contours
556 is 130°W (Fig. 8c). The maximum deepening of the NV19 storm occurred between
557 1700 UTC and 1800 UTC 26 November 2019 to the east of 130°W longitude. Out of
558 a combined 30-year period of northern Pacific Ocean EC events, no other EC event
559 has had a maximum deepening location as far east as the NV19 storm, yet another
560 aspect of its anomalous nature.



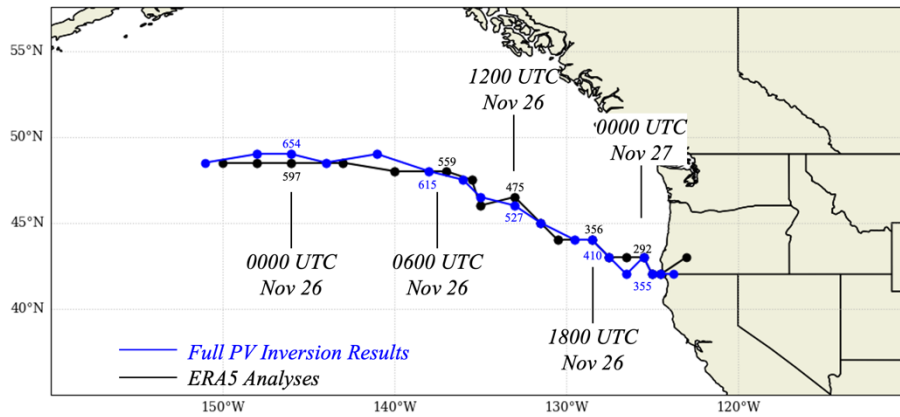
561

562 Fig. 8. Composite of maximum deepening locations (MDL) for “bomb” cyclogenesis events over
 563 the northeastern Pacific Ocean as defined by Sanders and Gyakum (1980) and Zhang et al. (2017).
 564 (a) Adapted from Roebber (1984) for MDL between 1976 and 1982. Red star indicates MDL for
 565 November 2019 storm. (b) Adapted from Wang and Rogers (2001) for MDL between 1985 and
 566 1996. Red star indicates MDL for November 2019 storm. (c) Adapted from Zhang et al. (2017) for
 567 MDL between 2000 and 2015. Red star indicates MDL for November 2019 storm. Dashed, gray
 568 line indicates 130°W meridian.

569 4. Analysis

570 Subsequent analysis will concentrate on the 950 hPa isobaric surface as this level
 571 was the lowest available isobaric surface in the inversion output. Figure 9 compares
 572 950 hPa geopotential height (Φ_{950}) at the location of the 950 hPa vorticity maximum
 573 of the NV19 storm from the ERA5 analyses and the full PV inversion. Though the full
 574 inversion results consistently return a higher Φ_{950} , the hourly positions demonstrate

575 excellent agreement. Results of inverting the 2-month mean PV are not discussed as
 576 the analysis is primarily concerned with the perturbation PV introduced into the
 577 domain by the NV19 storm.



578
 579 Fig. 9. Comparison of the full PV inversion results and the ECMWF reanalysis version 5 (ERA5)
 580 analysis of storm track based on location of the 950 hPa vorticity maxima. Location of vorticity
 581 maxima in the full PV inversion results are shown in blue with geopotential height at the vorticity
 582 maxima plotted in meters. Location of ERA5 analysis vorticity maxima are shown in black with
 583 geopotential height at the vorticity maxima plotted in meters.

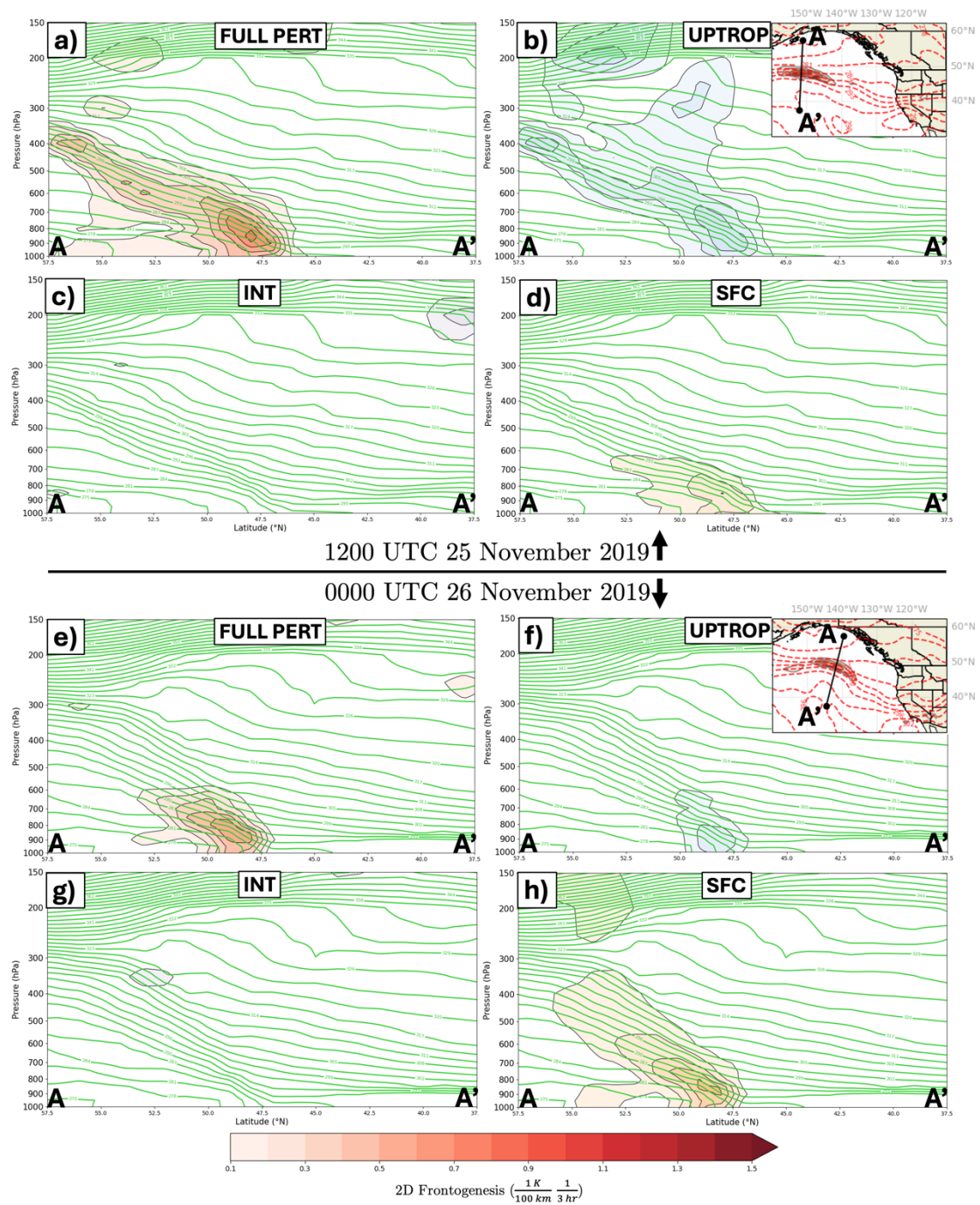
584 *a. Piecewise frontogenesis*

585 Piecewise PV inversion allows computation of the horizontal frontogenesis
 586 function (6) using the recovered balanced flow from the inversion of the full column
 587 perturbation PV and each of the three partitioned pieces of the perturbation PV. The
 588 goal is to determine which features in the perturbation PV distribution are controlling
 589 the strength and evolution of the initial lower-tropospheric frontogenesis (e.g. Korner
 590 and Martin 2000), as latent heat release within the thermally-direct circulation, in
 591 response to the intense lower-tropospheric frontogenesis, spawned the DRW which
 592 became the NV19 storm (Figs. 2d, 3d, 6). Therefore, we are only partitioning the
 593 balanced flow field, not the thermal field, and are considering the kinematic effects of
 594 the separate circulations on the total thermal field.

595 1) 1200 UTC 25 November 2019

596 Ascent during the initial development of the NV19 storm was situated on the
 597 warm side of a frontogenesis maximum at 850 hPa forced by differential θ advection

598 by the FULL PERT balanced flow (Fig. 10a). There is good agreement between the
599 distribution and orientation of the frontogenesis calculated using the FULL PERT
600 balanced flow and the frontogenesis calculated using the ERA5 horizontal winds
601 (compare Fig. 2d and Fig. 10a). A majority of the FULL PERT frontogenesis was
602 forced by the UPTROP PV balanced flow associated with the upstream upper-
603 tropospheric shortwave (Fig. 2f and 10b). The balanced flow associated with the INT
604 PV resulted in no notable frontogenesis along the cross section at this time (Fig. 10c).
605 A strong, negative INT PV anomaly in the upper-troposphere was located directly
606 above the development region (not shown) due to persistent, differential lower-
607 tropospheric high θ_e flow fueling convection along the baroclinic zone (e.g. Fig 6a).
608 Despite the emergence of a lower-tropospheric positive INT PV anomaly in response
609 to the associated heating, the negative (upper-tropospheric) piece of the INT PV
610 exerted the predominant influence on the total INT PV-induced flow in the
611 development region and, consequently, the INT PV contributed near-zero
612 frontogenesis (Fig. 10c). The remaining portion of the lower-tropospheric
613 frontogenesis was forced by the SFC PV balanced flow (Fig. 10d). This portion of
614 perturbation frontogenesis was a result of anomalously warm near-surface potential
615 temperatures underneath the 950 and 850 hPa thermal ridge stretching southwest of
616 the development region which facilitated strong differential warm air advection in the
617 lower-troposphere across the baroclinic zone (Fig. 2a,c).



618

619 Fig. 10. Frontogenesis associated with discrete portions of the balanced flow derived from
 620 piecewise PV inversion. (a) Cross section along A-A' in Fig. 2c of potential temperature and
 621 frontogenesis valid at 1200 UTC 25 November 2019. Potential temperature (green) contoured
 622 every 3 K starting at 300 K. Positive frontogenesis function from the full perturbation PV (FULL
 623 PERT) balanced flow (red shading) shaded every $1 \times 10^{-1} \text{ K (100km)}^{-1} (3\text{hr})^{-1}$ and smoothed
 624 using a 9-point smoother. (b) Cross section along A-A' in Fig. 2c of potential temperature and

625 frontogenesis valid at 1200 UTC 25 November 2019. Potential temperature (green) contoured
626 every 3 K starting at 300 K. Positive frontogenesis function from the UPTROP PV balanced flow
627 (blue shading) shaded every $1 \times 10^{-1} \text{ K (100km)}^{-1} (3\text{hr})^{-1}$ and smoothed using a 9-point
628 smoother. (c) As in panel (b) but for the positive frontogenesis function from the INT PV balanced
629 flow (pink shading). (d) As in panel (c) but for the positive frontogenesis function from the SFC
630 PV balanced flow (orange shading). (e) As in panel (a) but for a cross section along A-A' in Fig.
631 3c valid at 0000 UTC 26 November 2019. (f) As in panel (b) but for a cross section along A-A' in
632 Fig. 3c valid at 0000 UTC 26 November 2019. (g) As in panel (c) but for a cross section along A-
633 A' in Fig. 3c valid at 0000 UTC 26 November 2019. (h) As in panel (d) but for a cross section
634 along A-A' in Fig. 3c valid at 0000 UTC 26 November 2019.

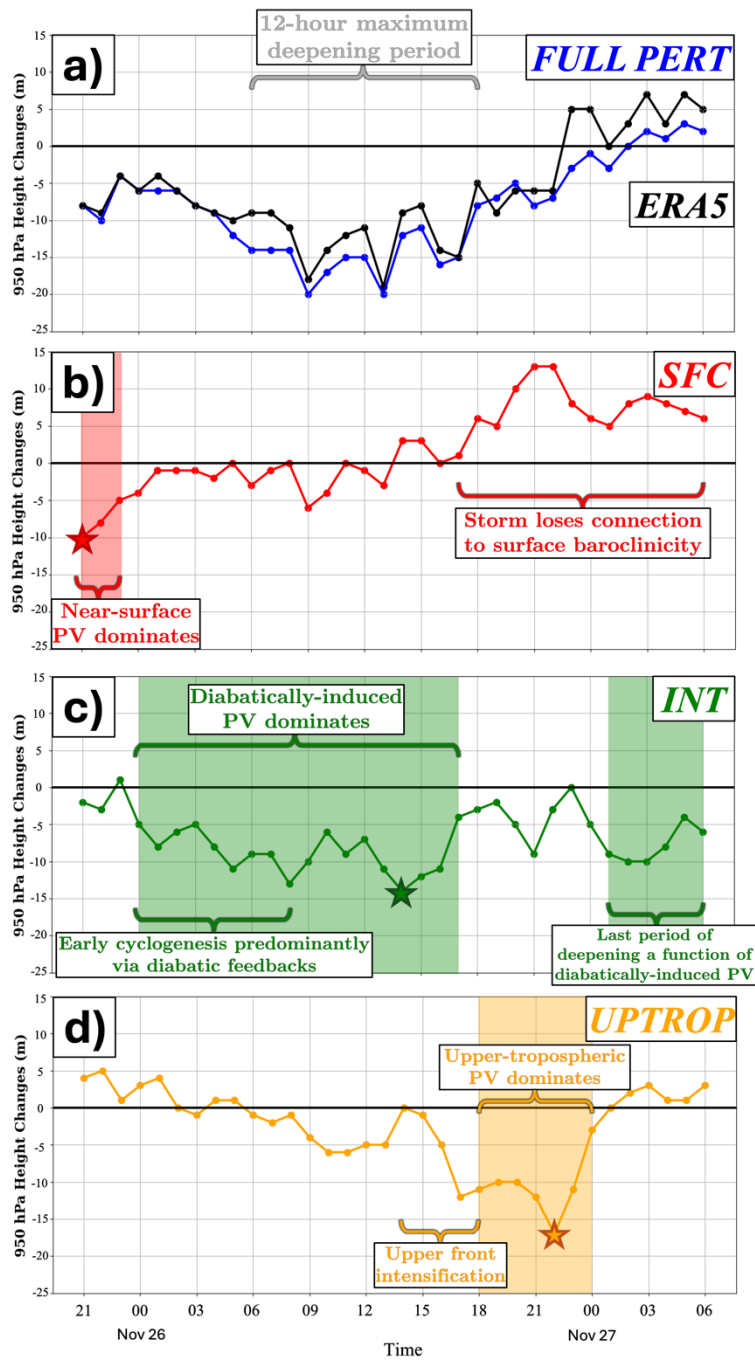
635 2) 0000 UTC 26 November 2019

636 The FULL PERT frontogenesis function became focused in the lower-troposphere
637 as the DRW vortex developed into a weak center of low pressure (Fig. 10e). There
638 was still good agreement between the frontogenesis calculated using the FULL PERT
639 balanced flow and the frontogenesis calculated using the ERA5 horizontal winds
640 (compare Fig. 3d and Fig. 10e). The perturbation frontogenesis forced by the
641 UPTROP PV balanced flow was now both shallower and weaker as compared to
642 twelve hours prior (Fig. 10b,f). The DRW was still situated beneath an upper-
643 tropospheric negative INT PV anomaly, and so the balanced flow from the INT PV
644 once again resulted in insubstantial perturbation frontogenesis (Fig. 10g). At this time,
645 the majority of the lower-tropospheric frontogenesis appeared forced by the balanced
646 flow attributable to lower-tropospheric potential temperature perturbations (Fig. 3a,c
647 and Fig. 10h). Perturbation southerly flow introduced via lower-tropospheric potential
648 temperature anomalies provided most of the lower-tropospheric frontogenesis and
649 subsequent latent heat release as NV19 DRW intensification and eastward
650 propagation began.

651 *b. Hourly height changes*

652 After a coherent lower-tropospheric vortex had formed, the intensification of the
653 NV19 storm was assessed by considering the effects of each of the three pieces of the
654 perturbation PV on near-surface height changes recovered from the piecewise PV

655 inversion process. First, perturbation heights from the ERA5, FULL PERT, UPTROP,
656 and SFC PV inversions, and the INT PV residual, were recorded at the location of the
657 950 hPa vorticity maximum associated with the NV19 storm. Then the perturbation
658 height change at time t , associated with the ERA5, full perturbation PV, and each of
659 the three pieces, was the result of subtracting the perturbation heights at time $t +$
660 $1hr$ from the perturbation heights at time $t - 1hr$ and dividing by the time interval of
661 $2 hrs$. The results of these calculations are shown in Fig. 11, which displays the
662 various height changes from 2100 UTC 25 November to 0600 UTC 27 November
663 2019.



664

665 Fig. 11. 950 hPa 1-hourly height changes from the inversion of the pieces of the perturbation PV
 666 at the location of the 950 hPa vorticity maximum of the November 2019 storm. (a) 950 hPa 1-
 667 hourly height changes from the inversion of the FULL PERT PV (blue) as defined in Section 3
 668 (see text) along with the observed ERA5 1-hourly height changes (black). Notable time period(s)
 669 are annotated. (b) As in (a) but for 1-hourly height changes associated with the SFC PV. Red
 670 shading indicates the time period in which the SFC PV contributed the most negative 950 hPa
 671 height changes of all three perturbation PV pieces. Red star indicates the time of most negative

672 950 hPa 1-hourly height change from the SFC PV inversion. (c) As in (b) but for 1-hourly height
673 changes associated with the INT PV. Green shading indicates time periods in which the INT PV
674 contributed the most negative 950 hPa height changes of all three perturbation PV pieces. Green
675 star indicates the time of most negative 950 hPa 1-hourly height change from the INT PV
676 inversion. (d) As in (c) but for 1-hourly height changes associated with the UPTROP PV. Orange
677 shading indicates the time period in which the UPTROP PV contributed the most negative 950
678 hPa height changes of all three perturbation PV pieces. Orange star indicates the time of most
679 negative 950 hPa 1-hourly height change from the UPTROP PV inversion.

680

681 Perturbation height changes from the ERA5 data and the inversion of the full
682 perturbation PV were negative at the location of the 950hPa vorticity maximum for a
683 majority of the 33-hour analysis period, with peak negative values occurring between
684 0900 UTC and 1300 UTC 26 November before exhibiting a steady increase until the
685 end of the analysis period (Fig. 11a). The ERA5 and the full perturbation PV
686 inversion height changes were in very good agreement. The 12-hour maximum
687 deepening period spanned from 0600 UTC to 1800 UTC 26 November, with the
688 storm having experienced consecutive MSLP falls greater than 1 hPa hr⁻¹ beginning at
689 0900 UTC 26 November until making landfall. The influence of surface potential
690 temperature anomalies on near-surface height changes were initially negative, and
691 then were negligible until the NV19 storm lost connection to surface baroclinicity
692 after 1600 UTC 26 November (Fig. 11b). Diabatically-induced PV had the most
693 dominant influence throughout an overwhelming majority of the development (Fig.
694 11c). Near-surface height changes associated with the INT PV residual were negative
695 beginning at 0000 UTC 26 November until the end of the storm lifecycle, including
696 throughout the entire 12-hour maximum deepening period. In fact, INT PV
697 contributed the most negative height changes during the early and late stages of
698 cyclogenesis (Fig. 11). The influence of the upper-tropospheric and stratospheric PV
699 (the UPTROP PV) on near-surface height changes was minimal until 1500 UTC 26
700 November, by which time the developing upper-level jet/front system had finally
701 encroached upon the NV19 storm, quickly inducing strong negative height changes
702 (Fig. 11d). These height changes were the most negative of any associated with the
703 three pieces of the perturbation PV directly outside of the 12-hour maximum

704 deepening period. Interrogations of the various physical mechanisms responsible for
705 this period of development, including potential interaction between the lower-
706 tropospheric DRW vortex and the upper-level jet/front system, which initially
707 developed independently of each other, will be explored separately in future work.

708 *c. Mutual amplification*

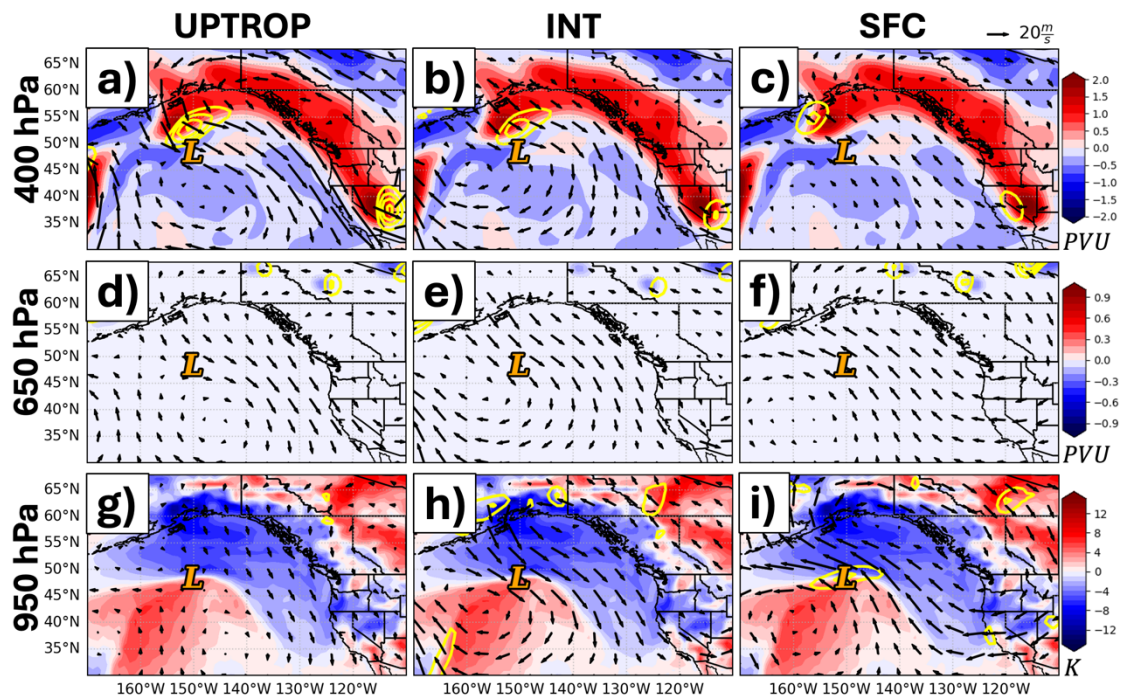
709 The influence of specific PV anomalies (i.e., UPTROP, INT, and SFC) on the
710 strength of the flow throughout the column is described via the PV superposition
711 principle (Davis and Emanuel 1991; Morgan and Nielsen-Gammon 1998). The
712 anomalous flow associated with, for instance, an UPTROP PV anomaly can interact
713 with the INT PV distribution (at a given isobaric level) to amplify the magnitude of
714 the INT PV anomaly via horizontal advection. In a statically stable atmosphere, local
715 increases in EPV translate to increases in cyclonic circulation. Additionally, positive
716 advection of lower boundary potential temperature anomalies by any discrete portion
717 of the balanced flow will induce similar increases in cyclonic circulation (Bretherton
718 1966). Therefore, any location experiencing positive advection of perturbation EPV
719 by a balanced flow, which would increase the anomalous EPV there, will also
720 experience an increase in the perturbation cyclonic circulation. Any such increase is a
721 manifestation of the PV superposition principle and is labeled mutual cyclonic
722 amplification.

723 The hour at which the associated perturbation height changes are most negative
724 for the UPTROP, INT, and SFC PV (indicated by the starred times in Figs. 11b-d) are
725 considered next. The analysis assesses if such favorable superposition amongst the
726 various balanced flows attributable to the UPTROP, INT, and SFC PV contributed to
727 an increase in the cyclonic flow throughout the column at these times during the
728 NV19 storm.

729 1) 2100 UTC 25 November 2019

730 The initial near-surface height changes of the NV19 storm, from 2100 UTC to
731 2300 UTC 25 November, were predominantly driven by the influence of lower-
732 boundary PV (Fig. 11b). The most negative of these 950 hPa height changes occurred

733 at 2100 UTC 25 November, which corresponds to the time of initial formation of the
734 SLP minimum which became the NV19 cyclone. Cyclonic PV advection (CPVA) by
735 the balanced flow at three different isobaric levels from the inversion of the UPTROP
736 and SFC PV and the INT PV residual at 2100 UTC 25 November are shown in Fig.
737 12. The yellow contours on each of the nine panels indicate where there is either
738 appreciable CPVA or positive surface potential temperature advection by the balanced
739 flow from a specified perturbation PV anomaly at the given isobaric level. In the
740 upper troposphere, the balanced flows from the UPTROP and INT resulted in CPVA
741 of upper-tropospheric PV to the north of the NV19 storm (Fig. 12a,b) while upper-
742 tropospheric CPVA from the SFC balanced flow was occurring well to the northwest
743 of the storm (Fig. 12c). No distinct diabatically-induced PV anomaly had formed in
744 the mid-troposphere early in the storm lifecycle, so no notable cyclonic advection of
745 this type of PV was occurring (Figs. 12d-f). Cyclonic advection of lower-boundary
746 PV by the UPTROP and INT balanced flows was not occurring in the vicinity of the
747 NV19 storm (Fig. 12g,h). Only the balanced flow from the SFC was resulting in
748 lower-boundary CPVA immediately over the NV19 storm center (Fig. 12i).
749 Therefore, at this early time in storm development, lower-boundary CPVA was being
750 amplified only by SFC anomalies and no substantial mutual cyclonic amplification of
751 PV anomalies throughout the depth of the troposphere was occurring.

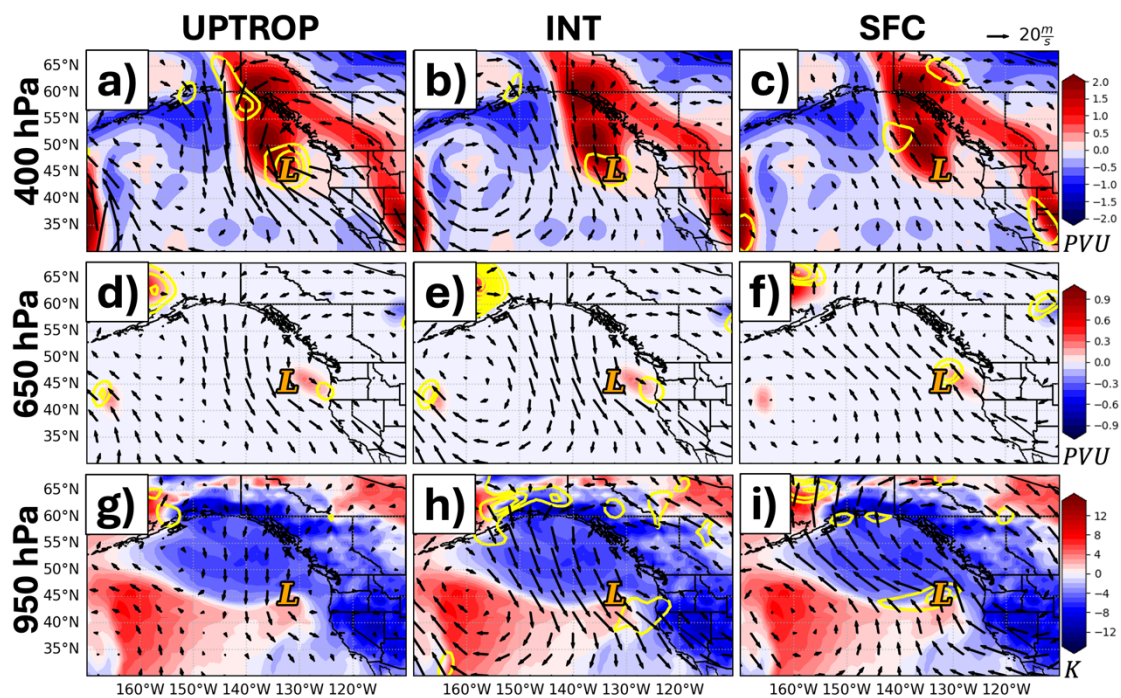


752

753 Fig. 12. Balanced flow attributable to the UPTROP, INT, and SFC perturbation PV and the
 754 influence of that balanced flow on the 3D PV and potential temperature anomaly structure valid at
 755 2100 UTC 25 November 2019. (a-c) 400 hPa UPTROP PV anomalies shaded every 0.25 PVU
 756 ($1 \text{ PVU} = 1 \times 10^{-6} \text{ m}^2 \text{ s}^{-1} \text{ K kg}^{-1}$) starting at 0.25 PVU and 400 hPa balanced flow (arrows) from
 757 the inversion of the (a) UPTROP, (b) INT, and (c) SFC. Yellow, solid contours represent positive
 758 UPTROP PV advection by the (a) UPTROP, (b) INT, and (c) SFC balanced flows contoured
 759 every 0.1 PVU hr^{-1} starting at 0.1 PVU hr^{-1} . Location of the 950 hPa relative vorticity maximum
 760 indicated by the orange 'L'. (d-f) 650 hPa INT PV anomalies shaded every 0.1 PVU starting at
 761 0.1 PVU and 650 hPa balanced flow (arrows) from the inversion of the (d) UPTROP, (e) INT, and
 762 (f) SFC. Yellow, solid contours represent positive INT PV advection by the (d) UPTROP, (e) INT,
 763 and (f) SFC balanced flows contoured every starting 0.1 PVU hr^{-1} at 0.1 PVU hr^{-1} . Location of the
 764 950 hPa relative vorticity maximum indicated by the orange 'L'. (g-i) 975 hPa potential
 765 temperature anomalies (SFC PV anomalies) shaded every 1 K and the 950 hPa balanced flow
 766 from the inversion of the (g) UPTROP, (h) INT, and (i) SFC as represented by the arrows. Yellow,
 767 solid contours represent positive surface potential temperature advection by the (g) UPTROP, (h)
 768 INT, and (i) SFC balanced flows contoured every 1 K hr^{-1} starting at 1 K hr^{-1} . Location of the
 769 950 hPa relative vorticity maximum indicated by the orange 'L'.

770 2) 1400 UTC 26 November 2019

771 A majority of the subsequent cyclogenesis in terms of 950 hPa height changes was
772 attributable to diabatically-induced PV, which dominated near-surface intensification
773 from 0000 UTC to 1600 UTC 26 November (Fig. 11c). Near-surface 1-hourly height
774 changes associated with the diabatically-induced PV were most negative at 1400 UTC
775 26 November, which was during the last hours of the 12-hour period of most rapid
776 deepening. At that time, the balanced flows from the inversion of the UPTROP and
777 INT residual were responsible for CPVA of upper-tropospheric PV directly over the
778 NV19 storm (Fig. 13a,b) while the balanced flow from the inversion of SFC induced
779 CPVA well to the northwest (Fig. 13c). By this time, diabatic heating had generated a
780 notable cyclonic mid-tropospheric PV anomaly due east of the surface cyclone.
781 CPVA by the UPTROP and INT balanced flows was occurring to the east-southeast
782 of the storm center (Fig. 13d,e). Advection of this mid-tropospheric PV by the
783 balanced SFC winds was also occurring directly northeast of the storm (Fig. 13f). No
784 appreciable advection of lower-boundary potential temperature by the UPTROP
785 winds was occurring at this time (Fig. 13g). The balanced flow attributable to the INT
786 resulted in lower-boundary CPVA to the southeast of the NV19 storm (Fig. 13h)
787 while the SFC winds resulted in lower-boundary CPVA directly over the NV19 storm
788 (Fig. 13i). Mutual cyclonic amplification throughout the column was ongoing at this
789 time as CPVA induced by both UPTROP and INT was occurring in the upper-
790 troposphere (Fig. 13a,b), CPVA induced by UPTROP, INT, and SFC was evident in
791 the mid-troposphere (Figs. 13d-f) and CPVA induced by INT and SFC was ongoing
792 in the lower-troposphere (Fig. 13h,i).



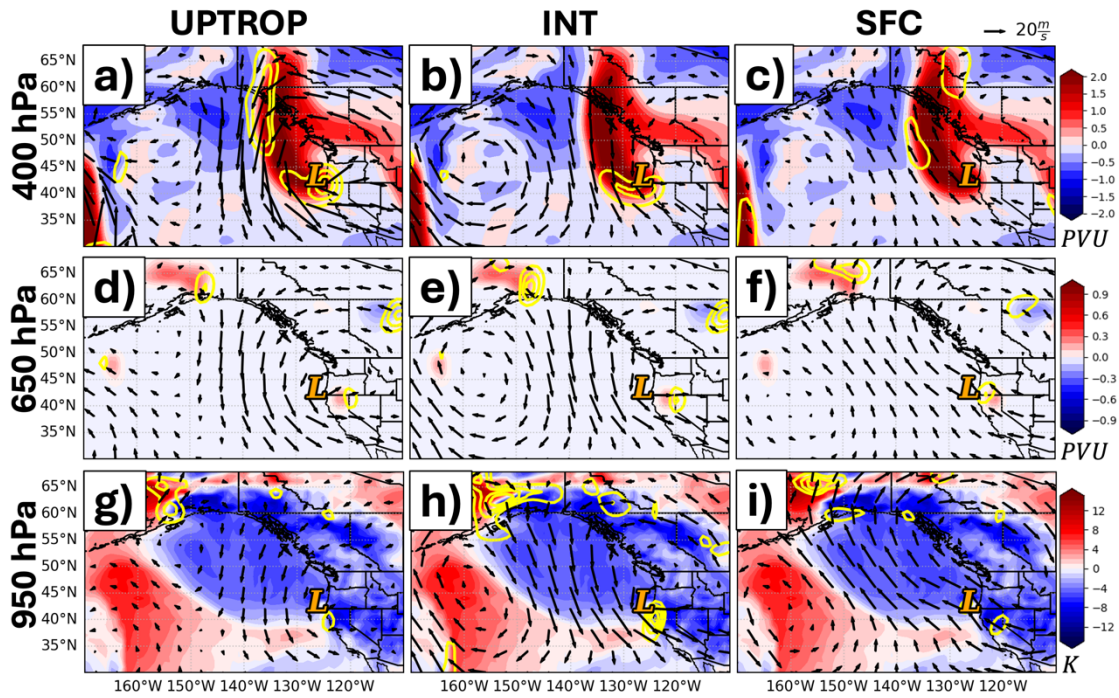
793

794 Fig. 13. (a) As in Fig. 12a except for 1400 UTC 26 November 2019. (b) As in Fig. 12b except for
 795 1400 UTC 26 November 2019. (c) As in Fig. 12c except for 1400 UTC 26 November 2019. (d) As
 796 in Fig. 12d except for 1400 UTC 26 November 2019. (e) As in Fig. 12e except for 1400 UTC 26
 797 November 2019. (f) As in Fig. 12f except for 1400 UTC 26 November 2019. (g) As in Fig. 12g
 798 except for 1400 UTC 26 November 2019. (h) As in Fig. 12h except for 1400 UTC 26 November
 799 2019. (i) As in Fig. 12i except for 1400 UTC 26 November 2019.

800 3) 2200 UTC 26 November 2019

801 Upper-tropospheric PV anomalies dominated near-surface development directly
 802 following the 12-hour most rapid deepening period of the NV19 storm (Fig. 11d).
 803 Near-surface 1-hourly height changes from the inversion of the UPTROP peaked at
 804 2200 UTC 26 November, which was nearly coincident with the time at which the
 805 upper-level jet/front system was most intense (not shown). At this time, the winds
 806 associated with UPTROP and INT induced CPVA to the east and south of the NV19
 807 storm, respectively (Fig. 14a,b). There was again no advection of upper-tropospheric
 808 PV by the SFC balanced flow near the storm at this time (Fig. 14c). Diabatically-
 809 induced PV anomalies in the mid-troposphere were weaker at this time, with mid-
 810 tropospheric CPVA from each piece of the perturbation flow occurring to the east of
 811 the storm center (Figs. 14d-f). Lower-boundary CPVA from the UPTROP and INT

812 balanced flows was situated to the southeast of the NV19 storm center (Fig. 14g,h)
 813 with no substantial lower-boundary CPVA arising from the SFC balanced flow (Fig.
 814 14i). Therefore, it appears that mutual cyclonic amplification was primarily occurring
 815 in the mid-troposphere (Figs. 14d-f) and upper-troposphere (Figs. 14a,b) late in the
 816 development of the cyclone.



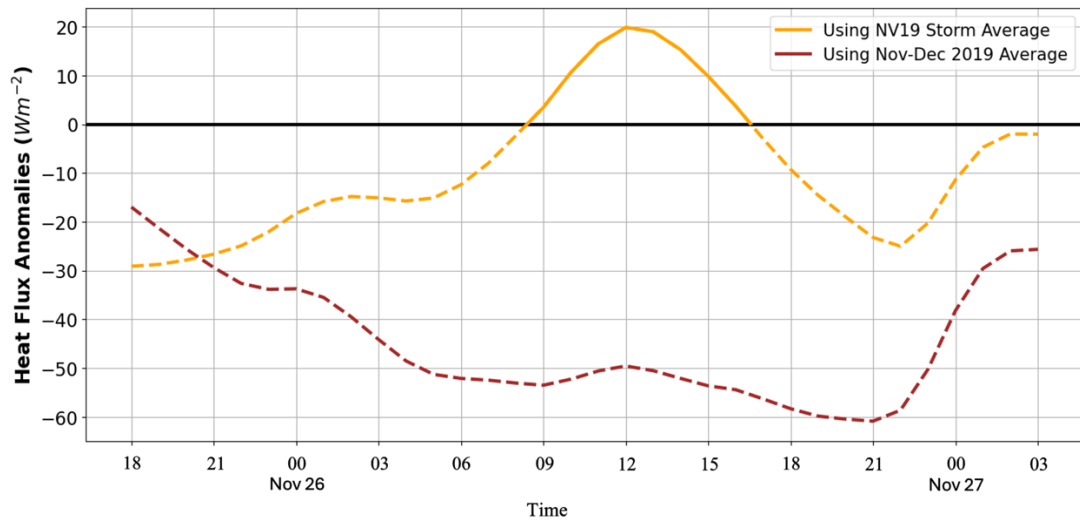
817
 818 Fig. 14. (a) As in Fig. 13a except for 2200 UTC 26 November 2019. (b) As in Fig. 13b except for
 819 2200 UTC 26 November 2019. (c) As in Fig. 13c except for 2200 UTC 26 November 2019. (d) As
 820 in Fig. 13d except for 2200 UTC 26 November 2019. (e) As in Fig. 13e except for 2200 UTC 26
 821 November 2019. (f) As in Fig. 13f except for 2200 UTC 26 November 2019. (g) As in Fig. 13g
 822 except for 2200 UTC 26 November 2019. (h) As in Fig. 13h except for 2200 UTC 26 November
 823 2019. (i) As in Fig. 13i except for 2200 UTC 26 November 2019.

824 *d. Summary*

825 The foregoing analysis reveals that the early propagation of the NV19 DRW was
 826 facilitated by column stretching tied to lower-tropospheric frontogenesis along the
 827 pre-existing baroclinic zone. This frontogenesis was predominantly forced by
 828 differential temperature advection associated with the UPTROP balanced flow at
 829 1200 UTC 25 November, and then by the SFC balanced flow at 0000 UTC 26
 830 November 2019, at the start of DRW intensification. Analysis of the near-surface

831 height changes suggests that the diabatically-induced INT PV was the most prominent
832 contributor to near-surface height changes during the intensification of the NV19
833 storm. The upper-tropospheric/lower-stratospheric UPTROP PV contributed the most
834 to near-surface height changes during the last 12 hours of storm intensification just
835 prior to landfall. The lower-tropospheric SFC PV influenced near-surface height
836 changes only very early in the development. Since the SFC PV isolates the effects of
837 lower-boundary θ anomalies, which are influenced by near-surface heat fluxes, the
838 piecewise PV inversion presented here suggests that such fluxes exerted only a
839 marginal influence on intensification of the NV19 storm.

840 This suggestion is supported by consideration of ERA5 surface sensible heat data
841 across a $10^\circ \times 10^\circ$ box centered on the NV19 MSLP minimum throughout its
842 evolution. Surface sensible heat flux anomalies are calculated with respect to two
843 different time means: 1) from 1200 UTC 25 November to 0000 UTC 28 November
844 2019, which captures the entire NV19 storm lifecycle, and 2) from 0000 UTC 01
845 November to 2300 UTC 31 December 2019, the 2-month time mean. Employing the
846 first time mean approach, surface sensible heat flux was anomalously negative
847 throughout the majority of the NV19 storm evolution and was only positive between
848 0900 and 1600 UTC 26 November 2019 (Fig. 15). Using the 2-month time mean,
849 anomalous surface sensible heat flux was negative throughout the entire NV19
850 lifecycle (Fig. 15). Thus, the surface sensible heat flux was anomalously negative for
851 at least a majority, or perhaps all, of the NV19 lifecycle. This marginal influence of
852 both near-surface and surface heat fluxes is a notable difference from previous
853 piecewise PV inversions of DRW explosive cyclogenesis events (Moore et al. 2008;
854 Rivière et al. 2010).



855

856 Fig. 15. Surface sensible heat flux anomalies ($W m^{-2}$) from 1800 UTC 25 November to 0300
 857 UTC 27 November 2019 averaged across a $10^{\circ} \times 10^{\circ}$ box centered on the NV19 storm. Surface
 858 sensible heat flux anomaly relative to the NV19 storm time mean (1200 UTC 25 November to
 859 0000 UTC 28 November 2019) is contoured in solid orange with negative surface sensible heat
 860 flux anomaly represented by dashed contours. Surface sensible heat flux anomaly relative to the 2-
 861 month time mean (0000 UTC 01 November to 2300 UTC 31 December 2019) is contoured in
 862 solid brown with negative surface sensible heat flux anomaly represented by dashed contours.

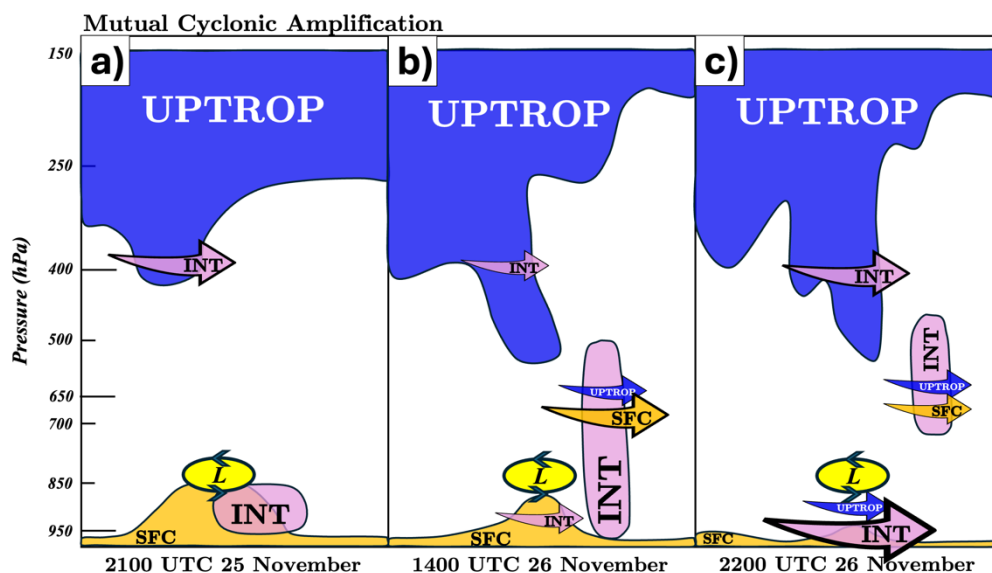
863

864 It is also suggested that mutual amplification between discrete pieces of
 865 perturbation PV progressed from the lower to the upper-troposphere as the NV19
 866 storm experienced a 29-hour period of uninterrupted 950 hPa height falls. This
 867 progression is visualized in schematic form in Fig. 16 with the colored illustrations
 868 representing each piece of the perturbation PV and similarly colored arrows indicating
 869 the strength and at which isobaric levels that piece of the perturbation PV contributed
 870 to mutual amplification.

871

872 Early in the lifecycle, only the balanced flow from the INT PV contributed to
 873 amplification of another PV anomaly, namely the UPTROP PV (Fig. 16a). Therefore,
 874 *mutual* amplification was relatively absent. As the storm began its period of rapid
 875 intensification, *mutual* amplification became more pervasive as the balanced flow
 876 associated with the UPTROP PV amplified the INT PV anomaly, the balanced flow
 877 associated with the INT PV amplified both the UPTROP PV and SFC PV anomalies,
 and the balanced flow associated with the SFC PV served to amplify the INT PV

878 anomaly (Fig. 16b). The mutual amplification signal at this time was strongest from
 879 the SFC PV. Towards the end of the rapid deepening period, the balanced flow
 880 associated with the SFC PV continued to amplify the INT PV anomaly, but the
 881 predominant mutual amplification involved the INT PV and UPTROP PV acting
 882 throughout the column (Fig. 16c). At this later time, the mutual amplification signal
 883 was strongest in association with the mid- to upper-tropospheric PV anomalies. The
 884 strength of the INT PV mutual amplification escalated as the NV19 storm matured
 885 and the influence of the UPTROP PV mutual amplification progressively extended
 886 throughout the whole depth of the troposphere (Fig. 16). The absence of an initial
 887 upper-tropospheric cyclogenetic precursor, coupled with the upward march of
 888 dominant developmental processes, suggests that the NV19 storm underwent a
 889 bottom-up development like that of *Lothar* (Wernli et al. 2002). Also, the NV19 storm
 890 propagated in the direction of the lower-tropospheric diabatically-generated PV
 891 anomaly which was located to the east (Figs. 13d-f) and southeast (Figs. 14d-f) of the
 892 cyclone center, fitting with the DRW propagation mechanism explained in Tamarin
 893 and Kaspi (2016) but with an equatorward rather than a poleward track.



894
 895 Fig. 16. Schematic of mutual cyclonic amplification during the development of the November
 896 2019 Northeast Pacific bomb cyclone. Orange, pink, and blue shapes represent the positive
 897 perturbation potential vorticity (PV) of the SFC, INT, and UPTROP PV, respectively, throughout
 898 the troposphere and lower stratosphere (see text for definition of SFC, INT, and UPTROP).

899 Orange, pink, and blue arrows indicate the perturbation balanced flow of the SFC, INT, and
900 UPTROP PV, respectively, which is resulting in mutual cyclonic amplification at a specific
901 isobaric level. Size of arrow indicates relative strength of mutual cyclonic amplification. Yellow
902 oval and “L” represents location of November 2019 Northeast Pacific bomb cyclone center. (a)
903 Mutual cyclonic amplification valid at 2100 UTC 25 November 2019. (b) Mutual cyclonic
904 amplification valid at 1400 UTC 26 November 2019. (c) Mutual cyclonic amplification valid at
905 2200 UTC 26 November 2019.

906 **5. Conclusions and Discussion**

907 Piecewise PV inversion of an extratropical cyclone in late November 2019 reveals
908 a case of explosive DRW development that was predominantly a function of the
909 influence of diabatic generation of PV associated with latent heat release. Only the
910 late stages of cyclogenesis were dominated by upper-tropospheric and lower-
911 stratospheric PV associated with an upper-level jet/front system. Analysis of the
912 piecewise frontogenesis, the 1-hourly height changes at the location of the 950 hPa
913 vorticity maximum, and mutual cyclonic amplification between perturbation PV
914 anomalies in different layers of the troposphere suggest that the NV19 storm followed
915 a bottom-up development similar to that described by Wernli et al. (2002) in
916 association with *Lothar*. The current study is, to the authors’ knowledge, unique in
917 that it interrogates the nature of an explosive DRW development over a cold ocean
918 surface.

919 Specific findings from the case study include:

- 920 1) The development of the NV19 storm was unusual in several ways; the storm
921 track was notably out of phase with other EC events in the northeast Pacific
922 Ocean and the typical DRW propagation direction, the deepening rate ranked
923 higher than the 90th percentile in two separate climatologies, and the maximum
924 deepening location of this storm occurred further east than any other EC event
925 over the northeast Pacific Ocean in a non-consecutive 30-year period.
- 926 2) Piecewise frontogenesis analysis, or frontogenesis calculated using the balanced
927 flows from the full column perturbation PV and the three partitioned pieces of
928 the perturbation PV, reveals that frontogenesis along the baroclinic zone
929 stretching across the northeast Pacific Ocean was predominantly a function of

930 balanced winds associated with the UPTROP PV prior to NV19 storm
931 formation and then almost entirely a function of balanced winds associated with
932 the SFC PV as the storm formed and began to strengthen. Thus, the dominant
933 forcing for the lower-tropospheric frontogenesis that mobilized the DRW was
934 transferred from the upper-troposphere prior to initial cyclogenesis to the
935 surface layer once more substantial development had begun.

936 3) Height falls associated with lower-tropospheric PV dominated in the very early
937 stages of cyclogenesis via the northward transport of high θ (θ_e) air along the
938 cold front of a cutoff cyclone situated to the west of an expansive anticyclone.
939 There was no signal of mutual cyclonic amplification between perturbation PV
940 anomalies throughout the troposphere during this initial formation as the lower-
941 tropospheric DRW formed.

942 4) Diabatic generation and rearrangement of PV throughout the depth of the
943 troposphere dominated near-surface height falls over the subsequent 16-hour
944 period. These diabatic feedbacks were in response to vigorous lower-
945 tropospheric frontogenesis which was situated along the warm front of the
946 NV19 storm. The diabatic feedbacks conspired to force mutual cyclonic
947 amplification of perturbation PV anomalies notably extending throughout the
948 depth of the troposphere. This period encompassed the entire 12-hour maximum
949 deepening period during which the storm deepened 34 hPa as it moved
950 southeastward.

951 5) The final period of development was dominated by upper-tropospheric PV
952 associated with an intense upper-level jet/front system which focused vigorous
953 CVA by the thermal wind directly over the surface cyclone as it approached the
954 coast. Mutual cyclonic amplification was primarily occurring between
955 perturbation PV anomalies in the mid- and upper-troposphere during this final
956 period of deepening.

957 6) The direct effects of near-surface heat fluxes, which are indirectly included in
958 the SFC PV by its definition, were quite unimportant to storm intensification in
959 this case of explosive DRW cyclogenesis. In fact, in contrast to previous
960 piecewise PV inversion studies on rapidly deepening DRWs (Moore et al. 2008;

961 Rivière et al. 2010), the SFC PV was the least important forcing for 950 hPa
962 height falls after the very initial stages of cyclogenesis. This result suggests that
963 explosive DRW developments over a cold ocean rely either on different
964 circumstances or a different sequencing of forcings than explosive DRWs that
965 develop over a warm ocean.

966 Like *Lothar*, the NV19 storm featured a bottom-up rapid intensification of a DRW
967 dependent upon diabatic generation of lower-tropospheric PV to spawn a potent
968 surface cyclone. DRW bottom-up rapid developments resemble the type-C
969 cyclogenesis events described in Plant et al. (2003) where cyclone intensification is
970 driven by latent heat release, with the addition of strong lower-tropospheric
971 baroclinicity (Boettcher and Wernli 2013; Tamarin and Kaspi 2016). Despite several
972 similarities, the NV19 storm did not follow the same developmental sequence as
973 *Lothar*. Wernli et al. (2002) showed that the circulation attributable to the lower-
974 tropospheric PV anomaly of *Lothar*, which was produced via intense latent heating,
975 was substantial enough to extend to the jet level and aid in the formation of an upper-
976 tropospheric PV anomaly which then further intensified the low-level PV anomaly
977 through PV superposition (Davis and Emanuel 1991; Morgan and Nielsen-Gammon
978 1998). Though the preceding analysis does not consider the problem directly, it
979 appears that both the lower- and upper-tropospheric PV anomalies associated with the
980 lower-tropospheric DRW vortex and upper-level jet/front system, respectively,
981 initially intensified independently of one another. Additionally, it does not appear that
982 the lower-tropospheric PV anomaly forced the development of the upper-tropospheric
983 PV anomaly, as was the case with *Lothar*, despite appearing to follow a similar
984 bottom-up development.

985 Systematic investigation of whether, and to what degree, the simultaneously
986 strengthening lower-tropospheric DRW vortex and upper-level jet/front system had
987 notable influences on one another during the NV19 development is a topic for future
988 work. Specific analysis will focus on whether the circulation associated with the
989 lower-tropospheric DRW vortex contributed to a mobilization of the “Shapiro effect”
990 (Rotunno et al. 1994) thereby instigating the development of the upper-level jet/front
991 system when the two features superposed. This proposition will be explored using

992 piecewise PV inversion in a forthcoming, complimentary study on this unusual
993 cyclogenesis event.

994 *Postscript.*

995 As the current study neared completion, a DRW over the northeastern Pacific
996 Ocean underwent explosive cyclogenesis from 1200 UTC 18 November to 0000 UTC
997 20 November 2024. This event displayed striking dynamical similarities to the event
998 presented in this paper, including a similar structural evolution and very rapid
999 intensification. At 1200 UTC 18 November, the cyclone developed along a zonally-
1000 oriented baroclinic zone which bisected an anticyclone over the northeast Pacific and
1001 was initially driven by lower-tropospheric latent heat release. By 0000 UTC 19
1002 November, an upper-tropospheric shortwave had moved into close proximity to the
1003 DRW and focused substantial CVA by the thermal wind (Sutcliffe 1947) over the
1004 cyclone center. In the subsequent 24 hours, the cyclone deepened an additional 66
1005 hPa, including a 26 hPa pressure fall between 1200 UTC and 1800 UTC 19
1006 November, matching the maximum 6-hour deepening rate accomplished by the *Braer*
1007 storm. The result was an impressive 945 hPa cyclone situated off the Washington,
1008 USA and British Columbia coastline.

1009 Both the NV19 storm and this recent event originated as innocuous-looking
1010 warm frontal waves, perhaps both as DRWs. Intense and geographically restricted
1011 lower-tropospheric frontogenesis produced heavy precipitation which, in turn,
1012 generated lower-tropospheric positive PV anomalies along the front. These anomalies
1013 orchestrated a period of modest growth before both cyclones were overtaken by
1014 potent tropopause-level disturbances which facilitated ascent and the stretching of
1015 vorticity-rich air that drove the rapid cyclogenesis.

1016 Further investigation of this extraordinary storm is ongoing with the goal of
1017 determining the physical importance of the similarities that appear to characterize
1018 these two extreme events.

1019

1020 *Acknowledgments.*

1021 The comments of three reviewers and two joint reviewers are appreciated and
1022 have greatly improved this manuscript. Chris Davis is acknowledged for developing
1023 the piecewise PV inversion code used in the analysis. This paper represents a portion

1024 of the first author's dissertation at the University of Wisconsin-Madison. The work
1025 was supported by the National Science Foundation under Grant AGS-1851152.

1026

1027 *Data Availability Statement.*

1028 The fifth generation ECMWF atmospheric reanalysis dataset (ERA5) is
1029 produced by the Copernicus Climate Change Service (C3S) at ECMWF and can be
1030 accessed via

1031 [https://cds.climate.copernicus.eu/cdsapp#!/dataset/10.24381/cds.143582cf?tab=overvi](https://cds.climate.copernicus.eu/cdsapp#!/dataset/10.24381/cds.143582cf?tab=overview)
1032 [ew](https://cds.climate.copernicus.eu/cdsapp#!/dataset/10.24381/cds.143582cf?tab=overview).

1033 Satellite imagery is produced by the National Centers for Environmental Information
1034 at NOAA and can be accessed via <https://www.ncei.noaa.gov/access>. Data used to
1035 make in Fig. 7 was adapted from Roebber (1984), Wang and Rogers (2001), and
1036 Zhang et al. (2017). All computer programs written to perform the data analysis are
1037 available from the authors upon request.

1038

REFERENCES

- 1039 Ahmadi-Givi, F., G. C. Graig, and R. S. Plant, 2004: The dynamics of a midlatitude cyclone with very
1040 strong latent-heat release. *Quart J Royal Meteoro Soc*, **130**, 295–323,
1041 <https://doi.org/10.1256/qj.02.226>.
- 1042 Boettcher, M., and H. Wernli, 2011: Life cycle study of a diabatic Rossby wave as a precursor to
1043 rapid cyclogenesis in the North Atlantic—Dynamics and forecast performance. *Monthly*
1044 *Weather Review*, **139**, 1861–1878.
- 1045 —, and —, 2013: A 10-yr climatology of diabatic Rossby waves in the Northern Hemisphere.
1046 *Monthly weather review*, **141**, 1139–1154.
- 1047 Bosart, L. F., 1981: The Presidents' Day snowstorm of 18–19 February 1979: A subsynoptic-scale
1048 event. *Monthly Weather Review*, **109**, 1542–1566.
- 1049 Bracegirdle, T. J., and S. L. Gray, 2009: The dynamics of a polar low assessed using potential
1050 vorticity inversion. *Quart J Royal Meteoro Soc*, **135**, 880–893,
1051 <https://doi.org/10.1002/qj.411>.
- 1052 Bretherton, F. P., 1966: Critical layer instability in baroclinic flows. *Quarterly Journal of the Royal*
1053 *Meteorological Society*, **92**, 325–334.
- 1054 Charney, J., 1955: The Use of the Primitive Equations of Motion in Numerical Prediction. *Tellus*, **7**,
1055 22–26, <https://doi.org/10.1111/j.2153-3490.1955.tb01138.x>.
- 1056 Davis, C. A., 1992: Piecewise potential vorticity inversion. *Journal of the atmospheric sciences*, **49**,
1057 1397–1411.
- 1058 —, and K. A. Emanuel, 1988: Observational evidence for the influence of surface heat fluxes on
1059 rapid maritime cyclogenesis. *Monthly Weather Review*, **116**, 2649–2659.
- 1060 —, and —, 1991: Potential vorticity diagnostics of cyclogenesis. *Monthly weather review*, **119**,
1061 1929–1953.
- 1062 Davis, C. A., E. D. Grell, and M. A. Shapiro, 1996: The Balanced Dynamical Nature of a Rapidly
1063 Intensifying Oceanic Cyclone. *Mon. Wea. Rev.*, **124**, 3–26, [https://doi.org/10.1175/1520-0493\(1996\)124<0003:TBDNOA>2.0.CO;2](https://doi.org/10.1175/1520-0493(1996)124<0003:TBDNOA>2.0.CO;2).
- 1064
- 1065 Ertel, H., 1942: Ein neuer hydrodynamischer wirbelsatz. *Meteorologische Zeitschrift*, **59**, 271–281.
- 1066 Fujiwhara, S., 1931: Short note on the behavior of two vortices. *Proceedings of the Physico-*
1067 *Mathematical Society of Japan. 3rd Series*, **13**, 106–110.
- 1068 Gyakum, J. R., and R. E. Danielson, 2000: Analysis of meteorological precursors to ordinary and
1069 explosive cyclogenesis in the western North Pacific. *Monthly Weather Review*, **128**, 851–
1070 863.
- 1071 —, P. J. Roebber, and T. A. Bullock, 1992: The role of antecedent surface vorticity development
1072 as a conditioning process in explosive cyclone intensification. *Monthly weather review*,
1073 **120**, 1465–1489.

- 1074 Heo, K.-Y., K.-J. Ha, and T. Ha, 2019: Explosive Cyclogenesis around the Korean Peninsula in May
1075 2016 from a potential vorticity perspective: case study and numerical simulations.
1076 *Atmosphere*, **10**, 322.
- 1077 Hersbach, H., and Coauthors, 2020: The ERA5 global reanalysis. *Quart J Royal Meteorol Soc*, **146**,
1078 1999–2049, <https://doi.org/10.1002/qj.3803>.
- 1079 Hoskins, B. J., M. E. McIntyre, and A. W. Robertson, 1985: On the use and significance of isentropic
1080 potential vorticity maps. *Quarterly Journal of the Royal Meteorological Society*, **111**, 877–
1081 946.
- 1082 Iizuka, S., M. Shiota, R. Kawamura, and H. Hatsushika, 2013: Influence of the monsoon variability
1083 and sea surface temperature front on the explosive cyclone activity in the vicinity of Japan
1084 during northern winter. *SOLA*, **9**, 1–4.
- 1085 Iwao, K., M. Inatsu, and M. Kimoto, 2012: Recent changes in explosively developing extratropical
1086 cyclones over the winter northwestern Pacific. *Journal of Climate*, **25**, 7282–7296.
- 1087 Kohl, M., and P. A. O’Gorman, 2022: The Diabatic Rossby Vortex: Growth Rate, Length Scale and
1088 the Wave-Vortex Transition. *Journal of the Atmospheric Sciences*,.
- 1089 Korner, S. O., and J. E. Martin, 2000: Piecewise frontogenesis from a potential vorticity perspective:
1090 Methodology and a case study. *Monthly Weather Review*, **128**, 1266–1288.
- 1091 Kouroutzoglou, J., H. Flocas, M. Hatzaki, K. Keay, I. Simmonds, and A. Mavroudis, 2015: On the
1092 dynamics of a case study of explosive cyclogenesis in the Mediterranean. *Meteorology
1093 and Atmospheric Physics*, **127**, 49–73.
- 1094 Kuo, Y.-H., S. Low-Nam, and R. J. Reed, 1991: Effects of surface energy fluxes during the early
1095 development and rapid intensification stages of seven explosive cyclones in the western
1096 Atlantic. *Monthly Weather Review*, **119**, 457–476.
- 1097 Lackmann, G. M., D. Keyser, and L. F. Bosart, 1997: A Characteristic Life Cycle of Upper-
1098 Tropospheric Cyclogenetic Precursors during the Experiment on Rapidly Intensifying
1099 Cyclones over the Atlantic (ERICA). *Mon. Wea. Rev.*, **125**, 2729–2758,
1100 [https://doi.org/10.1175/1520-0493\(1997\)125<2729:ACLCOU>2.0.CO;2](https://doi.org/10.1175/1520-0493(1997)125<2729:ACLCOU>2.0.CO;2).
- 1101 Lagouvardos, K., V. Kotroni, and E. Defer, 2007: The 21–22 January 2004 explosive cyclogenesis
1102 over the Aegean Sea: Observations and model analysis. *Quarterly Journal of the Royal
1103 Meteorological Society: A journal of the atmospheric sciences, applied meteorology and
1104 physical oceanography*, **133**, 1519–1531.
- 1105 Lang, A. A., and J. E. Martin, 2012: The structure and evolution of lower stratospheric frontal zones.
1106 Part 1: Examples in northwesterly and southwesterly flow. *Quarterly Journal of the Royal
1107 Meteorological Society*, **138**, 1350–1365.
- 1108 Lim, E.-P., and I. Simmonds, 2002: Explosive cyclone development in the Southern Hemisphere and
1109 a comparison with Northern Hemisphere events. *Monthly Weather Review*, **130**, 2188–
1110 2209.

- 1111 Martin, J. E., 2014: Quasi-geostrophic diagnosis of the influence of vorticity advection on the
 1112 development of upper level jet-front systems. *Quarterly Journal of the Royal*
 1113 *Meteorological Society*, **140**, 2658–2671.
- 1114 —, and J. A. Otkin, 2004: The rapid growth and decay of an extratropical cyclone over the central
 1115 Pacific Ocean. *Weather and forecasting*, **19**, 358–376.
- 1116 McKenzie, M. W., 2014: *An analysis of numerical weather prediction of the diabatic Rossby Vortex*.
 1117 NAVAL POSTGRADUATE SCHOOL MONTEREY CA,.
- 1118 Moore, R. W., and M. T. Montgomery, 2004: Reexamining the dynamics of short-scale, diabatic
 1119 Rossby waves and their role in midlatitude moist cyclogenesis. *Journal of the atmospheric*
 1120 *sciences*, **61**, 754–768.
- 1121 —, and —, 2005: Analysis of an idealized, three-dimensional diabatic Rossby vortex: A
 1122 coherent structure of the moist baroclinic atmosphere. *Journal of the atmospheric*
 1123 *sciences*, **62**, 2703–2725.
- 1124 —, —, and H. C. Davies, 2008: The integral role of a diabatic Rossby vortex in a heavy snowfall
 1125 event. *Monthly weather review*, **136**, 1878–1897.
- 1126 Morgan, M. C., and J. W. Nielsen-Gammon, 1998: Using tropopause maps to diagnose midlatitude
 1127 weather systems. *Monthly weather review*, **126**, 2555–2579.
- 1128 Odell, L., P. Knippertz, S. Pickering, B. Parkes, and A. Roberts, 2013: The Braer storm revisited.
 1129 *Weather*, **68**, 105–111.
- 1130 Parker, D. J., and A. J. Thorpe, 1995: Conditional convective heating in a baroclinic atmosphere: A
 1131 model of convective frontogenesis. *Journal of the atmospheric sciences*, **52**, 1699–1711.
- 1132 Plant, R., G. C. Craig, and S. Gray, 2003: On a threefold classification of extratropical cyclogenesis.
 1133 *Quarterly Journal of the Royal Meteorological Society: A journal of the atmospheric*
 1134 *sciences, applied meteorology and physical oceanography*, **129**, 2989–3012.
- 1135 R. B. Weldon, 1979: Cloud patterns and the upper air wind field, Part IV. National Weather Service
 1136 Satellite training note.
- 1137 Raymond, D., and H. Jiang, 1990: A theory for long-lived mesoscale convective systems. *Journal of*
 1138 *Atmospheric Sciences*, **47**, 3067–3077.
- 1139 Reed, R. J., and M. D. Albright, 1986: A case study of explosive cyclogenesis in the eastern Pacific.
 1140 *Monthly Weather Review*, **114**, 2297–2319.
- 1141 Rivière, G., P. Arbogast, K. Maynard, and A. Joly, 2010: The essential ingredients leading to the
 1142 explosive growth stage of the European wind storm Lothar of Christmas 1999. *Quarterly*
 1143 *Journal of the Royal Meteorological Society: A journal of the atmospheric sciences, applied*
 1144 *meteorology and physical oceanography*, **136**, 638–652.
- 1145 Roebber, P. J., 1984: Statistical analysis and updated climatology of explosive cyclones. *Monthly*
 1146 *Weather Review*, **112**, 1577–1589.

- 1147 —, 1989: The role of surface heat and moisture fluxes associated with large-scale ocean current
1148 meanders in maritime cyclogenesis. *Monthly weather review*, **117**, 1676–1694.
- 1149 —, 1993: A diagnostic case study of self-development as an antecedent conditioning process in
1150 explosive cyclogenesis. *Monthly weather review*, **121**, 976–1006.
- 1151 Rossby, C.-G., 1940: Planetary flow pattern in the atmosphere. *Quart. J. Roy. Meteor. Soc.*, **66**, 68–
1152 87.
- 1153 Rotunno, R., W. C. Skamarock, and C. Snyder, 1994: An analysis of frontogenesis in numerical
1154 simulations of baroclinic waves. *Journal of Atmospheric Sciences*, **51**, 3373–3398.
- 1155 Sanders, F., 1986: Explosive cyclogenesis in the west-central North Atlantic Ocean, 1981–84. Part
1156 I: Composite structure and mean behavior. *Monthly weather review*, **114**, 1781–1794.
- 1157 —, and J. R. Gyakum, 1980: Synoptic-dynamic climatology of the “bomb.” *Monthly Weather*
1158 *Review*, **108**, 1589–1606.
- 1159 Shapiro, M. A., 1981: Frontogenesis and Geostrophically Forced Secondary Circulations in the
1160 Vicinity of Jet Stream-Frontal Zone Systems. *J. Atmos. Sci.*, **38**, 954–973,
1161 [https://doi.org/10.1175/1520-0469\(1981\)038<0954:FAGFSC>2.0.CO;2](https://doi.org/10.1175/1520-0469(1981)038<0954:FAGFSC>2.0.CO;2).
- 1162 —, 1983: Mesoscale weather systems of the central United States. The national STORM
1163 program: Scientific and technological bases and major objectives. UCAR Rep. *Cooperative*
1164 *Institute for Research in Environmental Sciences*, **78**.
- 1165 Snyder, C., and R. S. Lindzen, 1991: Quasi-geostrophic wave-CISK in an unbounded baroclinic shear.
1166 *Journal of Atmospheric Sciences*, **48**, 76–86.
- 1167 Sutcliffe, R., 1947: A contribution to the problem of development. *Quarterly Journal of the Royal*
1168 *Meteorological Society*, **73**, 370–383.
- 1169 Tamarin, T., and Y. Kaspi, 2016: The poleward motion of extratropical cyclones from a potential
1170 vorticity tendency analysis. *Journal of the Atmospheric Sciences*, **73**, 1687–1707.
- 1171 Terpstra, A., T. Spengler, and R. W. Moore, 2015: Idealised simulations of polar low development
1172 in an Arctic moist-baroclinic environment. *Quarterly Journal of the Royal Meteorological*
1173 *Society*, **141**, 1987–1996.
- 1174 Wang, C.-C., and J. C. Rogers, 2001: A composite study of explosive cyclogenesis in different sectors
1175 of the North Atlantic. Part I: Cyclone structure and evolution. *Monthly Weather Review*,
1176 **129**, 1481–1499.
- 1177 Wernli, H., S. Dirren, M. A. Liniger, and M. Zillig, 2002: Dynamical aspects of the life cycle of the
1178 winter storm ‘Lothar’(24–26 December 1999). *Quarterly Journal of the Royal*
1179 *Meteorological Society: A journal of the atmospheric sciences, applied meteorology and*
1180 *physical oceanography*, **128**, 405–429.
- 1181 Winters, A. C., and J. E. Martin, 2017: Diagnosis of a North American polar–subtropical jet
1182 superposition employing piecewise potential vorticity inversion. *Monthly Weather*
1183 *Review*, **145**, 1853–1873.

- 1184 Yoshiike, S., and R. Kawamura, 2009: Influence of wintertime large-scale circulation on the
1185 explosively developing cyclones over the western North Pacific and their downstream
1186 effects. *Journal of Geophysical Research: Atmospheres*, **114**.
- 1187 Zhang, G., and Z. Wang, 2018: North Atlantic extratropical Rossby wave breaking during the warm
1188 season: Wave life cycle and role of diabatic heating. *Monthly Weather Review*, **146**, 695–
1189 712.
- 1190 Zhang, S., G. Fu, C. Lu, and J. Liu, 2017: Characteristics of explosive cyclones over the Northern
1191 Pacific. *Journal of Applied Meteorology and Climatology*, **56**, 3187–3210.
- 1192